# Regulation of apical constriction via microtubule- and Rab11-dependent apical transport during tissue invagination

Thao Phuong Le[1] and SeYeon Chung[1, *]

[1] Department of Biological Sciences, Louisiana State University, Baton Rouge, LA 70803, USA

[*]Author for correspondence: seyeonchung@lsu.edu

Running Head: MTs and Rab11 regulate apical constriction

Abbreviations: Crb, Crumbs; E-Cad, E-Cadherin; Dhc64C, Dynein heavy chain 64C; Fog, Folded gastrulation; GFP, green fluorescent protein; Klar, Klarsicht; MT, microtubule; Nuf, Nuclear fallout; Rok, Rho-associated kinase; SG, salivary gland; WT, wild type; YFP, yellow fluorescent protein.

## Abstract

The formation of an epithelial tube is a fundamental process for organogenesis. During *Drosophila* embryonic salivary gland (SG) invagination, Folded gastrulation (Fog)-dependent Rho-associated kinase (Rok) promotes contractile apical myosin formation to drive apical constriction. Microtubules (MTs) are also crucial for this process and are required for forming and maintaining apicomedial myosin. However, the underlying mechanism that coordinates actomyosin and MT networks still remains elusive. Here, we show that MT-dependent intracellular trafficking regulates apical constriction during SG invagination. Key components involved in protein trafficking, such as Rab11 and Nuclear fallout (Nuf), are apically enriched near the SG invagination pit in a MT-dependent manner. Disruption of the MT networks or knockdown of *Rab11* impairs apicomedial myosin formation and apical constriction. We show that MTs and Rab11 are required for apical enrichment of the Fog ligand and the continuous distribution of the apical determinant protein Crumbs (Crb) and the key adherens junction protein E-Cadherin (E-Cad) along junctions. Targeted knockdown of *crb* or *E-Cad* in the SG disrupts apical myosin networks and results in apical constriction defects. Our data suggest a role of MT- and Rab11-dependent intracellular trafficking in regulating actomyosin networks and cell junctions, to coordinate cell behaviors during tubular organ formation.

41 **Introduction**

42 Formation of three-dimensional tubes by invagination of flat epithelial sheets is a
43 fundamental process in forming organs such as the lungs and kidneys (Andrew and
44 Ewald, 2010). To enter the third dimension, cells must change their shapes and positions
45 relative to each other. A major cellular process during epithelial tube formation is apical
46 constriction, a universal cell shape change that is linked to tissue bending, folding and
47 invagination (Sawyer *et al.*, 2010; Martin and Goldstein, 2014). During apical constriction,
48 the apical side of an epithelial cell constricts, causing a columnar or cuboidal cell to
49 become wedge-shaped (Sawyer *et al.*, 2010; Martin and Goldstein, 2014). Manipulation
50 of apical constriction in a group of cells impacts both local and global tissue shape directly,
51 suggesting a critical role for apical constriction in forming proper tissue architecture
52 (Guglielmi *et al.*, 2015; Chung *et al.*, 2017; Izquierdo *et al.*, 2018).

53 Apical constriction is driven by actin filament (F-actin) networks and the molecular motor
54 non-muscle myosin II (hereafter referred to as myosin). Over the past decade, important
55 functions of different actomyosin structures in epithelial tissue morphogenesis have been
56 discovered. Particularly, studies in *Drosophila* revealed a distinct population of pulsatile
57 apical medial actomyosin (hereafter referred to as apicomedial myosin) that generates a
58 pulling force that exerts on adherens junctions to drive apical constriction (Martin *et al.*,
59 2009; Rauzi *et al.*, 2010; Booth *et al.*, 2014; Chung *et al.*, 2017). Further studies in early
60 *Drosophila* embryos discovered that apicomedial myosin is created in response to
61 signaling by the Folded gastrulation (Fog) ligand and its G protein-coupled receptors
62 (GPCRs) (Manning *et al.*, 2013; Kerridge *et al.*, 2016) and is regulated by apical Rho-
63 associated kinase (Rok) (Mason *et al.*, 2013).

64 Apical junctions and apical determinants also have an important role in the formation of
65 functional actomyosin complexes during developmental processes. During *Drosophila*
66 dorsal closure, the apical polarity regulators Par-6, aPKC and Bazooka/Par3 (Baz/Par3)
67 (altogether known as the Par complex) regulate pulsed actomyosin contractions in
68 amnioserosa cells (David *et al.*, 2010). In the *Drosophila* embryonic trachea, the apical

protein Crumbs (Crb) is required for proper organization of the actomyosin complex (Letizia *et al.*, 2011).

Emerging evidence suggests that microtubules (MTs) play a critical role in tissue invagination (Booth *et al.*, 2014; Ko *et al.*, 2019). MTs serve as tracks in intracellular transport (Le Droguen *et al.*, 2015; Khanal *et al.*, 2016; Aguilar-Aragon *et al.*, 2020), raising the possibility that MTs regulate apical constriction through the endo- and exocytosis of membrane receptors and adhesion molecules. Several lines of evidence also suggest the importance of the endocytic pathway in apical constriction in both in vitro and in vivo systems. In *Drosophila* S2 cells, RhoGEF2 travels to the cell cortex by interaction with the MT plus-end protein EB1 to stimulate cell contraction (Rogers *et al.*, 2004). During *Xenopus* gastrulation, disrupting endocytosis with dominant-negative dynamin or Rab5 perturbs apical constriction and invagination of cell sheets (Lee and Harland, 2010). During *Drosophila* gastrulation, the apical surface of cells is reshaped via Rab35 and RabGEF Sbf, which direct the plasma membrane to Rab11-positive recycling endosomes through a dynamic interaction with Rab5 endosomes to reshape actomyosin networks (Miao *et al.*, 2019). Moreover, in the developing neural tube in *Xenopus*, asymmetric enrichment of Rab11 at the medial apical junctions is critical for apical constriction, suggesting that membrane trafficking has a key role in apical constriction (Ossipova *et al.*, 2014). However, exactly how vesicle trafficking, MTs, and actomyosin networks are linked during tissue invagination remains to be discovered.

To determine how these three cellular attributes contribute to tissue invagination, we use the *Drosophila* embryonic SG as a model. We and others showed that apical constriction is regulated in a highly coordinated and spatiotemporally controlled manner during SG tube formation (Myat and Andrew, 2000; Booth *et al.*, 2014; Chung *et al.*, 2017; Sanchez-Corrales *et al.*, 2018). The *Drosophila* embryo forms two SG tubes via invagination of two epithelial placodes on the ventral surface (Myat and Andrew, 2002; Chung *et al.*, 2014). Before invagination, a small group of cells in the dorsal/posterior region of each SG placode begin to constrict. As those cells internalize to form the invagination pit, more cells anterior to the pit undergo clustered apical constriction in a Fog signaling-dependent manner (Chung *et al.*, 2017) (Figure 1A). In the absence of *fog*, SG cells fail to accumulate

Rok and myosin in the apicomedial region of the cells (Chung *et al.*, 2017). MTs aid in forming and maintaining the apicomedial myosin network during SG invagination (Booth *et al.*, 2014). The MT cytoskeleton near the invagination pit forms a network of longitudinal MT bundles, with the minus ends of MTs facing the apical domain of the cells and interacting with the apicomedial myosin (Booth *et al.*, 2014). Disruption of MTs causes loss of apicomedial myosin and disrupted apical constriction during SG invagination (Booth *et al.*, 2014). However, it is still unknown how intracellular trafficking affects these two processes.

In this study, we demonstrate that key proteins involved in intracellular trafficking - including Rab11, its binding partner Nuclear fallout (Nuf), and dynein heavy chain - are enriched in the apical domain of SG cells during invagination. Moreover, disruption of MTs results in mislocalization of Rab11 to the basolateral region of SG cells. Reducing *Rab11* in the SG leads to a decrease and dispersal of Rok and myosin in the apical domain and causes uncoordinated apical constriction. Our data suggest that apical localization of the Fog ligand, the apical determinant protein Crb, and the key adherens junction protein E-Cadherin (E-Cad) is compromised when the MT networks are disrupted or *Rab11* is knocked down. We further show that reducing *crb* or *E-Cad* in the SG leads to defects that are reminiscent of *Rab11* knockdown. Altogether, our work mechanistically links MT- and Rab11-dependent intracellular trafficking to the regulation of actomyosin networks during tubular organ formation.

## Results

### Intracellular trafficking components are apically enriched near the invagination pit

To test a role for the intracellular trafficking machinery in spatially biased signaling activation and protein accumulation during SG invagination, we analyzed the subcellular localization of proteins involved in vesicle trafficking in the SG. Several endosome markers and their interacting partners were tested, including Rab5 (an early endosome marker) (Gorvel *et al.*, 1991), Rab7 (a late endosome marker) (Wichmann *et al.*, 1992;

127 Meresse *et al.*, 1995), Rab11 (a recycling endosome marker) (Ullrich *et al.*, 1996),
128 Nuclear fallout (Nuf, a putative binding partner for Rab11) (Riggs *et al.*, 2003), and Sec15
129 (an exocyst complex component and effector for Rab11) (Zhang *et al.*, 2004; Langevin *et*
130 *al.*, 2005). Using labeling with E-Cad, an adherens junction marker, and CrebA, a SG
131 nuclear marker, we segmented apical cell outlines and calculated the intensity mean of
132 fluorescence signals of each endosomal marker. We observed apical enrichment of
133 several of them in the SG, including Rab11 and Nuf (Figure 1, B-B’’’’’). Similar enrichment
134 of Rab11 signals was also observed in the endogenously tagged Rab11 protein (Rab11-
135 EYFP; (Dunst *et al.*, 2015) (Supplemental Figure S1, A-A’’’’). Importantly, the enrichment
136 of Rab11 was more pronounced in the SG over time (Figure 1, D-F’’’’). Before
137 invagination, only low levels of Rab11 were detected in the apical domain of all SG cells
138 throughout the entire SG placode (Figure 1, D-D’’’’). Stronger signals of Rab11 were soon
139 detected in the SG as cells begin to undergo apical constriction in the dorsal/posterior
140 region of the placode (Figure 1, E-E’’’’), which intensified as invagination proceeded
141 (Figure 1, F-F’’’’). Quantification of the total intensity of Rab11 in the whole SG placode
142 showed significantly higher levels of Rab11 in invaginating SGs compared to before
143 invagination (Figure 1H), suggesting upregulated Rab11 levels in SG cells during
144 invagination. Furthermore, compared to before invagination (Figure 1G, top), intensity
145 mean of Rab11 in the apical domain of each cell showed a stronger negative correlation
146 with the apical area of cells in the entire SG during invagination (Figure 1G, bottom),
147 suggesting a close link between intracellular trafficking activities and apical constriction.

148 EYFP-tagged Rab5, an early endosome marker, was also enriched in the apical domain
149 in the invaginating SG, suggesting active endocytosis in the apical domain during SG
150 invagination (Supplemental Figure S1, B-B’’’). Rab7, a late endosome marker, however,
151 did not show apical enrichment but localized as large punctate structures in the cytoplasm
152 of the entire SG placode (Supplemental Figure 1, D-D’’’). Dynein heavy chain 64C, a
153 subunit of the dynein motor complex that transports cargos along MTs toward their minus
154 ends, also showed apical enrichment (Figure 1, C-C’’’). This is consistent with the
155 previous report that the minus end of MTs faces the apical domain of SG cells near the
156 invagination pit (Booth *et al.*, 2014). Sec15, an exocyst complex component, also showed
157 similar apical enrichment (Supplemental Figure S1, E-E’’’). Similar to Rab11 (Figure 1G),

158 intensity mean of Rab5-EYFP and Sec15 in the apical domain of each cell showed a
159 negative correlation with the apical area of cells in the entire SG during invagination
160 (Supplemental Figure S1, C and F). Compared to a more uniform distribution of other
161 endosomal markers in the entire apical domain of SG cells, Sec15 signals appeared to
162 be enriched at adherens junctions (Supplemental Figure S1E'). Overall, our results
163 suggest active intracellular trafficking, possibly both endo- and exocytosis, in the apical
164 domain of SG cells near the invagination pit during invagination.

165

166 **Apical enrichment of Rab11 and Nuf is MT-dependent**

167 Strong apical enrichment of Rab11 and other trafficking components in SG cells near the
168 invagination pit led us to test whether these vesicle markers are associated with vertically
169 aligned MTs that could facilitate their polarized distribution. As in many epithelial cells,
170 MT minus- and plus-ends face the apical and the basal domain of the SG cells,
171 respectively (Myat and Andrew, 2002; Booth *et al.*, 2014). Indeed, co-immunostaining of
172 tyrosinated α-tubulin, a marker of dynamic or newly polymerized MTs (Westermann and
173 Weber, 2003), and Rab11 showed a partial overlap of the two proteins at the apical region
174 of the SG cells (Figure 2, A-B'').

175 To test whether Rab11 apical enrichment in SG cells is dependent on MT networks, we
176 disrupted MTs in the SG by overexpressing spastin, a MT-severing protein (Sherwood *et*
177 *al.*, 2004), using the SG-specific *fkh-Gal4* driver. In control SGs, tyrosinated α-tubulin and
178 acetylated α-tubulin, a marker of stable and longer-lived MTs (Westermann and Weber,
179 2003), were observed abundantly in the apical domain of cells in the whole placode
180 (Figure 2, C'' and C'''; Supplemental Figure S2A''). In spastin-overexpressing SGs, both
181 tyrosinated and acetylated α-tubulin signals were strongly reduced, revealing a loss of
182 MT filaments (Booth *et al.*, 2014) (Figure 2, D'' and D''' and Supplemental Figure S2B'').
183 Compared to control, spastin-overexpressing SGs showed cells with extremely small or
184 large apical areas (Supplemental Figure S2, C-E). Cells with small apical areas were
185 distributed randomly throughout the SG placode, rather than clustered as in control SGs
186 (Supplemental Figure S2, C and D). The apical enrichment of Rab11 (Figure 2C') was

also disrupted and Rab11 was mislocalized basolaterally (Figure 2D'). SGs with disrupted MTs showed much lower Rab11 and Nuf intensity in the apical domain compared to control SGs (Figure 2, E-G). To compare the relative variability of apical enrichment of Rab11/Nuf in WT and spastin-overexpressing SGs, we calculated the degree of variability, the ratio of the deviation of Rab11/Nuf intensity to the mean Rab11/Nuf intensity. Compared to WT, spastin-overexpressing SGs showed a lower degree of relative variability of intensity (Figure 2G). These data suggest that apical Rab11/Nuf signals are less varied from cell to cell regardless of apical areas of individual cells in spastin-overexpressing SGs. Overall, these data suggest that MT networks are required for apical enrichment of Rab11 and Nuf during SG invagination.

**Rab11 and dynein functions are required for apical constriction in the SG**

We next asked if modulation of Rab11 levels could compromise apical constriction. To test this possibility, we disrupted the function of Rab11 in the SG by either overexpressing a dominant-negative form of Rab11 (Rab11S25N-YFP; (Zhang *et al.*, 2007); hereafter referred to as Rab11-DN) or knocking down *Rab11* using RNAi lines. Reduced Rab11 levels upon *Rab11* knockdown were confirmed using a Rab11 antibody in both stage 11 and stage 13 SGs (Supplemental Figure S3, A-D'). SGs that were invaginated within the range of 5.1- 9.9 μm depth were used for quantification for proper comparison between different genotypes. Compared to control (Figure 3A), SGs overexpressing Rab11-DN or knocking down *Rab11* showed more cells with larger apical areas (Figure 3, B, C and F), suggesting a role for Rab11 in apical constriction during SG invagination.

As dynein heavy chain was also enriched apically in the SG during invagination (Figure 1, C' and C'''), we tested if dynein function is also required for apical constriction during SG invagination. Indeed, knockdown of *Dynein heavy chain 64C* (*Dhc64C*) in the SG using RNAi resulted in more cells with larger apical areas during invagination, suggesting defective apical constriction upon *Dhc64C* knockdown (Figure 3, D, D' and G). As dynein binds to and clusters the minus ends of microtubules (Heald *et al.*, 1996; Khodjakov *et al.*, 2003; Goshima *et al.*, 2005; Burbank *et al.*, 2006; Elting *et al.*, 2014; Tan *et al.*, 2018),

216 we asked if *Dhc64C* knockdown affects the MT networks in the SG. Knocking down
217 *Dhc64C* in the SG resulted in a slight reduction of tyrosinated α-tubulin (Figure 3J'). These
218 data suggest that apical constriction defects observed in *Dhc64C* knockdown are, at least
219 in part, due to affected MT networks.

220 Klarsicht (Klar), the *Drosophila* Klarsicht-Anc-Syne Homology (KASH) domain protein,
221 mediates apical transport in the SG (Myat and Andrew, 2002) via the MT motor
222 cytoplasmic dynein (Gross *et al.*, 2000). We therefore tested if *klar* also influences apical
223 constriction during SG invagination. *klar* null mutant embryos showed SGs with mild
224 apical constriction defects compared to wild type (Figure 3, E-F' and H). Importantly,
225 unlike *Dhc64C* knockdown, no significant difference in the MT networks was observed in
226 SGs in *klar* mutants (Figure 3L'), suggesting that apical constriction defects in *klar*
227 mutants are due to disrupted apical transport. Overall, our data suggest essential roles of
228 MT-, Rab11- and dynein-dependent intracellular transport in regulating apical constriction
229 during SG invagination.

230

231 **Reduced Rab11 function leads to the reduction of apicomedial myosin formation**
232 **and failure in accumulation of apicomedial Rok in SG cells**

233 The apicomedial myosin structure generates the pulling force to drive apical constriction
234 in SG cells (Booth *et al.*, 2014; Chung *et al.*, 2017). Disruption of MTs by spastin
235 overexpression inhibits formation of apicomedial myosin during SG invagination (Booth
236 *et al.*, 2014). To test whether apicomedial myosin is affected in SG cells when *Rab11* is
237 knocked down, we measured the overall intensity of myosin in the apicomedial region of
238 SG cells using sqh-GFP, a functional GFP-tagged version of the myosin regulatory light
239 chain (Royou *et al.*, 2004). In control SGs, sqh-GFP showed strong myosin signals with
240 clear web-like structures in the apicomedial region of cells near the invagination pit
241 (Figure 4, A-A''''). Knockdown of *Rab11*, however, caused a significant reduction of
242 apicomedial myosin intensity in SG cells in the same area (Figure 4, B-B'''' and C).
243 Moreover, unlike clear web-like structures of apicomedial myosin in control SGs (Figure
244 4, A''-A''''), myosin was more dispersed and fragmented in *Rab11* RNAi SGs (Figure 4,

245 B''-B''''), resulting in a decrease in areas of myosin accumulation in the apicomedial
246 region of SG cells (Figure 4E). These data suggest roles for Rab11 in both upregulating
247 apical myosin and forming and/or maintaining apicomedial myosin web.

248 We also tested whether junctional myosin, a myosin pool closely associated with
249 adherens junctions in SG cells, is affected in *Rab11* RNAi SGs. Consistent with previous
250 studies (Roper, 2012; Chung *et al.*, 2017), junctional myosin showed strong signals in
251 wild type SG cells, often with stronger signals at vertices (Figure 4A'''). Intriguingly, the
252 junctional myosin intensity slightly increased when *Rab11* was knocked down (Figure 4,
253 B''' and D). The ratio of apicomedial to junctional myosin intensity was significantly
254 reduced in *Rab11* RNAi SGs (Figure 4D), suggesting an imbalance of contractile forces
255 in the SG.

256 We previously showed that accumulation of apicomedial Rok is required for apicomedial
257 myosin formation for coordinated apical constriction in SG cells (Roper, 2012; Chung *et*
258 *al.*, 2017). To test whether Rok accumulation is dependent on Rab11, we quantified
259 accumulation of apicomedial Rok-GFP signals using a ubiquitously expressed GFP-
260 tagged Rok transgene (Rok-GFP; (Abreu-Blanco *et al.*, 2014) in wild type and *Rab11*
261 RNAi SGs (Figure 4, F-G''). Indeed, the reduction of *Rab11* levels led to more dispersed
262 Rok signals along the apical domain of SG cells near the pit (Figure 4H). Overall, our data
263 suggest Rab11-dependent apical apicomedial myosin formation and accumulation of Rok
264 during SG invagination.

265

266 **Reduced dynein function leads to failure in proper organization of apicomedial**
267 **myosin in SG cells**

268 We next tested whether apicomedial myosin formation is affected in *Dhc64C* RNAi and
269 *klar* mutant SGs. Despite the slight disruption of the MT networks in *Dhc64C* RNAi SGs
270 (Figure 3J'), the overall intensity of apicomedial or junctional myosin was not significantly
271 changed in *Dhc64C* RNAi SGs (Figure 5C), suggesting that subtle defects in the MT
272 networks do not affect apical upregulation of myosin. Similar to *Dhc64C* knockdown, no

273 significant difference in the intensity of apicomedial and junctional myosin was observed
274 in *klar* mutant SGs (Figure 5H). However, the ratio of apicomedial to junctional myosin
275 was reduced in both genotypes (Figure 5, D and I). Moreover, the area of apicomedial
276 myosin accumulation was significantly reduced in *Dhc64C* RNAi or *klar* mutant SGs
277 (Figure 5, E and J), suggesting defects in forming proper apicomedial myosin web in
278 these genotypes. Our data suggest that defective apical constriction in *Dhc64C* RNAi and
279 *klar* mutant SGs could be due to failure in proper organization of myosin structures in SG
280 cells.

281 We also tested for accumulation of apicomedial Rok-GFP signals in spastin-
282 overexpressing, *Dhc64C* RNAi and *klar* mutant SGs. Disruption of MTs by spastin
283 overexpression abolished apicomedial accumulation of Rok in cells near the invagination
284 pit (Figure 5, L' and P), found in control SGs (Figure 5K'). Reduction of *Dhc64C* levels
285 also led to more dispersed Rok signals along the apical domain of SG cells near the pit
286 (Figure 5, M' and P). In *klar* mutants, Rok-GFP tended to accumulate less profoundly and
287 less uniformly in the apicomedial region of SG cells (Figure 5O') although not statistically
288 significant compared to control (Figure 5Q). Overall, our data suggest that MT- and
289 dynein-dependent apical accumulation of Rok and apicomedial myosin formation during
290 SG invagination.

291

292 **MT- and Rab11-dependent apical enrichment of Fog, Crb and E-Cad is required for**
293 **apical constriction during SG invagination**

294 We next tested potential cargos of MT- and Rab11-dependent apical transport during SG
295 invagination. Rok accumulation, apicomedial myosin formation and subsequent clustered
296 apical constriction in the SG is dependent on Fog signaling (Chung *et al.*, 2017). We
297 therefore tested if apical transport of the Fog ligand is MT- and Rab11-dependent.
298 Staining using an antibody against Fog in control SGs showed upregulated Fog signals
299 in the apical domain of SG cells (Figure 6, A-A'''). However, in spastin-overexpressing or
300 *Rab11* RNAi SGs, apical Fog signals were reduced (Figure 6, B-C'''). To compare apical
301 enrichment of Fog between WT and spastin-overexpressing or *Rab11* RNAi SGs, we

302 calculated the overall intensity of apical Fog signals in the entire SG placode in
303 corresponding genotypes. Compared to control, Fog levels in the apical domain of the
304 SG were reduced when spastin was overexpressed or *Rab11* was knocked down (Figure
305 6D). We also calculated the degree of variability, the ratio of the deviation of Fog intensity
306 to the mean intensity of Fog in the SG. Compared to WT, spastin-overexpressing or
307 *Rab11 RNAi* SGs had a lower degree of relative variability of intensity (Figure 6E). These
308 data suggest that apical Fog signals are less varied from cell to cell regardless of apical
309 areas when MTs are disrupted or Rab11 function is reduced. Overall, these data suggest
310 that apical transport of Fog in the SG is dependent on the MT networks and Rab11.

311 We further tested MT- and Rab11-dependent apical transport of other apical and
312 junctional proteins during SG invagination. Transport of several key apical and junctional
313 proteins is dependent on MTs and Rab11 (Le Droguen *et al.*, 2015; Khanal *et al.*, 2016;
314 Jouette *et al.*, 2019). One such protein is an apical transmembrane protein Crb, and
315 Rab11 helps maintain apical Crb in the *Drosophila* ectoderm (Roeth *et al.*, 2009). In the
316 *Drosophila* SG and follicle cells, Crb is apically transported along MTs by the dynein motor
317 (Myat and Andrew, 2002). Importantly, in *Drosophila* tracheae, loss of *crb* impairs apical
318 constriction during the internalization process (Letizia *et al.*, 2011). The key junctional
319 protein E-Cad is also trafficked by MTs in *Drosophila* embryonic trachea (Le Droguen *et*
320 *al.*, 2015). During apical constriction, contractile forces generated by the actomyosin
321 complex are exerted on adherens junctions, with E-Cad being a core component that
322 integrates contractile forces to generate tension (Martin *et al.*, 2009).

323 We therefore asked if MTs and Rab11 have roles in apical distribution of Crb and E-Cad
324 in the SG during invagination. Compared to control (Figure 6, F' and F'''), spastin-
325 overexpressing SG cells showed discontinuous Crb signals (Figure 6, G' and G''').
326 Although the number of gaps was not significantly different between control and spastin-
327 overexpressing SGs (Figure 6J), the ratio of the length of gap over junctional length was
328 significantly increased in SGs that overexpress spastin (Figure 6I). Unlike for Crb,
329 disruption of MTs in the SG did not cause obvious gaps in E-Cad signals at adherens
330 junctions compared to control (Figure 6, F'', F'''', G'' and G''''). However, we observed an
331 ununiform distribution of E-Cad signals along adherens junctions in spastin-

332 overexpressing SGs (Figure 6G’’’’). The degree of variability of E-Cad intensity along the
333 junctions was significantly increased in spastin-overexpressing SGs compared to control
334 (Figure 6K). Importantly, *Rab11* knockdown resulted in similar discontinuous Crb and
335 uneven E-Cad signals (Figure 6, H-H’’’’, I and K). These data suggest that proper apical
336 distribution of Crb and E-Cad in the invaginating SG is dependent on MTs and Rab11.

337 To test for roles of Crb and E-Cad in regulating apical constriction during SG invagination,
338 we knocked down either gene in the SG using RNAi. Knockdown of *crb* or *E-Cad* resulted
339 in the reduction of junctional Crb or E-Cad levels, respectively, compared to control
340 (Supplemental Figure S3, E-F’’). Reduction of *crb* increased the number of cells with
341 larger apical areas compared to control (Figure 7, A, B and D). Quantification of the
342 percentage of cells and cumulative percentage of cells of different apical areas showed
343 a significant decrease in the number of constricting cells in *crb* knockdown SGs (Figure
344 7D). *E-Cad* knockdown SGs also displayed a similar trend, although with less statistical
345 significance (Figure 7, C and D). These data suggest roles for Crb and E-Cad, with more
346 subtlety for E-Cad, in regulating apical constriction during SG invagination.

347

348 **Apical localization of Fog, Crb and E-Cad is MT- and Rab11-dependent in the SG**
349 **throughout development**

350 To further investigate the role of MTs in Rab11-dependent apical trafficking during SG
351 development, we overexpressed spastin in the SG throughout development and analyzed
352 late stage SGs. Analysis of spastin-overexpressing SGs at stage 16 revealed that
353 disruption of MTs resulted in short SG tubes with a thin lumen compared to control SGs
354 of the same stage (Supplemental Figure S4, A and B). Strikingly, whereas the majority of
355 Rab11- and Nuf-positive vesicles localized in the apical region of control SG cells
356 (Supplemental Figure S4, A-A’’’), Rab11 and Nuf were observed as large aggregates in
357 the cytoplasm in spastin-overexpressing cells, overlapping with each other (Supplemental
358 Figure S4, B-B’’’). Our data suggest that MTs are required for apical enrichment of
359 Rab11/Nuf vesicles throughout SG tube formation.

360 We next tested whether MTs and Rab11 are required for apical transport of Fog, Crb and
361 E-Cad also at later stages. Compared to the control SG (Supplemental Figure S4C''),
362 apical Fog signals were significantly reduced in SGs that overexpress spastin or knock
363 down *Rab11* (Supplemental Figure S4, D'' and E''), suggesting that Fog is trafficked
364 apically in a MT- and Rab11-dependent manner in the SG throughout tube formation. No
365 significant changes were detected in apical Crb localization in SGs that overexpress
366 spastin or knock down *Rab11* (data not shown). Compared to strong E-Cad enrichment
367 in adherens junctions in control SG cells (Supplemental Figure S4C'), SGs that
368 overexpress spastin or knock down *Rab11* showed stronger E-Cad signals in the lateral
369 domain of cells (Supplemental Figure S4, D' and E').

370 To further test MT-dependent apical transport of Crb or E-Cad in the SG, we used a
371 genetic suppression strategy in the overexpression background: we co-overexpressed
372 Crb or E-Cad along with spastin in the SG to test whether disruption of MTs affects apical
373 transport of Crb or E-Cad. A similar approach was taken in a recent study, where
374 overexpression of Crb provided a highly sensitive genetic background for identifying
375 components involved in Crb trafficking (Aguilar-Aragon *et al.*, 2020). Consistent with
376 previous studies (Wodarz *et al.*, 1993; Chung and Andrew, 2014), Crb overexpression in
377 the SG caused a dramatic increase of the apical membrane as well as mislocalization of
378 Crb basolaterally along the entire membrane (Supplemental Figure S4, F-F'). Co-
379 overexpression of spastin along with Crb suppressed the overexpression phenotypes for
380 Crb (Supplemental Figure S4, G-G'). E-Cad overexpression in the SG caused
381 mislocalization of E-Cad as punctate structures in the basolateral region (Supplemental
382 Figure S4, H'-H''). Importantly, in SGs that co-overexpressed spastin along with Crb or
383 E-Cad, each protein mislocalized as cytoplasmic aggregates near the basolateral domain,
384 which were largely overlapping with mislocalized Rab11/Nuf (Supplemental Figure S4,
385 G'-G''' and I'-I'''). Overall, our data suggest that Fog, Crb and E-Cad are trafficked apically
386 in a MT- and Rab11-dependent manner in the SG throughout tube formation.

387

388 **Reducing apical and junctional proteins affects apicomedial myosin formation**

389 To test whether apical constriction defects observed in *crb* and *E-Cad* RNAi SGs are
390 linked to apicomedial myosin formation, we quantified myosin levels and areas of
391 apicomedial myosin in SGs with these knockdowns. Compared to control SGs (Figure 8,
392 A-A''), *crb* RNAi SGs showed a slight decrease in apicomedial myosin levels (Figure 8,
393 B-B'' and D). No significant difference in the junctional myosin intensity was observed in
394 *crb* RNAi SGs (Figure 8, B-B'' and D). The ratio of apicomedial to junctional myosin was
395 reduced (Figure 8E), suggesting that apical constriction defects in SGs depleted of *crb*
396 are, at least in part, due to failure of apicomedial myosin formation. Supporting this idea,
397 areas of apicomedial myosin web-like structures were significantly reduced in *crb* RNAi
398 SGs compared to WT (Figure 8F).

399 In SGs knocked down *E-Cad*, myosin levels at each domain did not change significantly
400 (Figure 8, C-C'' and E), but areas of apicomedial myosin web-like structures were
401 significantly decreased (Figure 8F). The ratio of apicomedial to junctional myosin was
402 also significantly reduced in *E-Cad* RNAi SGs compared to control (Figure 8, C-C'' and
403 E). Therefore, apical constriction defects caused by *E-Cad* knockdown might be due to
404 defective apicomedial myosin formation and the imbalance of contractile forces.

405 Consistent with reduced apicomedial myosin (Figure 8, B' and D), knockdown of *crb* also
406 resulted in Rok-GFP signals less accumulating in the apical region of cells near the
407 invagination pit (Figure 8, F-G'). Quantification of areas occupied by Rok-GFP puncta
408 showed significant reduction in accumulation of apicomedial Rok when *crb* was knocked
409 down (Figure 8I). Consistent with little effect of *E-Cad* knockdown on apicomedial myosin
410 intensity (Figure 8, C-C'' and E), Rok accumulation was not significantly affected by *E-*
411 *Cad* knockdown (Figure 8, H-H' and I). Taken together, our results suggest a role for Crb
412 in regulating apical constriction by apicomedial myosin activation during SG invagination.

413

414 **Discussion**

415 **MTs and Rab11 regulate Fog signaling activity during SG invagination**

416 MTs have a crucial role in stabilizing apical myosin during epithelial morphogenesis both
417 in early *Drosophila* embryos and in the *Drosophila* SG (Booth *et al.*, 2014; Ko *et al.*, 2019).
418 In the SG, MTs interact with apicomedial myosin via Short stop, the *Drosophila*
419 spectraplakin, emphasizing a direct interplay between the MT and the apical myosin
420 networks (Booth *et al.*, 2014). Our data reveals another key role of MTs in regulating
421 protein trafficking to control the apical myosin networks during tissue invagination. During
422 SG invagination, a network of longitudinal MT bundles is observed near the invagination
423 pit (Booth *et al.*, 2014). Our data shows apical enrichment of Rab11 in the same area is
424 MT-dependent (Figures 1 and 2) and that this enrichment is important for forming the
425 apicomedial myosin networks (Figure 4), suggesting a link between localized intracellular
426 trafficking along MTs to apical myosin regulation.

427 The dorsal/posterior region of the SG, where Rab11 is apically enriched in a MT-
428 dependent manner (Figures 1 and 2), correlates with localized Fog signaling activity that
429 promotes clustered apical constriction (Chung *et al.*, 2017). Disruption of MTs or *Rab11*
430 knockdown reduces Fog signals in the apical domain of SG cells (Figure 6) and causes
431 dispersed Rok accumulation and defective apicomedial myosin formation (Figure 4). It is
432 consistent with our previous study that the absence of Fog signal results in dispersed
433 apical Rok and defects in apicomedial myosin formation (Chung *et al.*, 2017). We
434 therefore propose that MT- and Rab11-dependent apical trafficking regulates Fog
435 signaling activity to control apical constriction during epithelial tube formation, through
436 transporting the Fog ligand. As recycling of membrane receptors to the cell surface plays
437 an important role in regulating overall signaling activity, it is possible that Rab11 is
438 involved in recycling the as yet unidentified SG receptor(s) of Fog to regulate Fog activity
439 in the SG. Indeed, several GPCRs are recycled via Rab11 (Anborgh *et al.*, 2000;
440 Innamorati *et al.*, 2001; Hunyady *et al.*, 2002; Volpicelli *et al.*, 2002; Fan *et al.*, 2003; Dale
441 *et al.*, 2004; Hamelin *et al.*, 2005; Cerniello *et al.*, 2017). During epithelial invagination in
442 early *Drosophila* embryogenesis, the concentration of the Fog ligand and receptor
443 endocytosis by β-arrestin-2 have been shown as coupled processes to set the amplitude
444 of apical Rho1 and myosin activation (Jha *et al.*, 2018). It is possible that the movement
445 of Fog receptor(s) that have internalized as a stable complex with β-arrestin is recycled

446 back to the cell surface by Rab11. The Fog signaling pathway represents one of the best-
447 understood signaling cascades controlling epithelial morphogenesis (Manning and
448 Rogers, 2014). Although best studied in *Drosophila*, the pathway components have also
449 been identified in other insects, suggesting a more widely conserved role of Fog signaling
450 in development (Urbansky *et al.*, 2016; Benton *et al.*, 2019). Further work needs to be
451 done to fully understand the regulatory mechanisms underlying the trafficking of Fog and
452 its receptor(s) during epithelial morphogenesis.

453 Our analysis of apicomedial myosin shows that reduced Rab11 function not only causes
454 a decrease of the myosin intensity but also causes myosin to be dispersed rather than
455 forming proper myosin web structures in the apicomedial domain of SG cells (Figure 4).
456 These data support the idea that Rab11 function is required for both concentration and
457 spatial organization of apicomedial myosin. This can be explained by the combined effect
458 of multiple cargos that are transported by Rab11, including Fog, Crb and E-Cad (as
459 discussed below). Time-lapse imaging of myosin will help determine how the dynamic
460 behavior of apicomedial myosin is compromised when Rab11 function is disrupted.

461

462 **Integrating apical and junctional proteins with actomyosin networks during SG**
463 **invagination**

464 During branching morphogenesis in *Drosophila* trachea, MTs and dynein motors have a
465 critical role in the proper localization of junctional proteins such as E-Cad (Le Droguen *et*
466 *al.*, 2015). This is consistent with our observations with MT-dependent uniform distribution
467 of E-Cad at adherens junctions in the invaginating SG (Figure 6), suggesting a conserved
468 role of MT-dependent intracellular trafficking in junctional remodeling and stabilization
469 during epithelial tube formation. Our data further suggest that the MT networks and Rab11
470 have key roles in apical distribution of Crb and E-Cad in the SG (Figure 6) and that proper
471 levels of apical and junctional proteins are important for apical constriction during SG
472 invagination (Figure 7). Based on these data, we propose that MT- and Rab11-dependent
473 apical trafficking of Crb and E-Cad is critical for apical constriction during SG invagination.
474 Alternatively, MTs have an additional role in assembling/anchoring these apical

475 components, through the regulation of unidentified molecules. Recent studies in
476 *Drosophila* mesoderm invagination showed that MTs help establish actomyosin networks
477 linked to cell junction to facilitate efficient force transmission to promote apical constriction
478 (Ko *et al.*, 2019). In (Ko *et al.*, 2019), however, MT-interfering drugs and RNAi of CAMSAP
479 end-binding protein were used to prevent MT functions and the effect cannot be directly
480 compared to our data where spastin was used to sever existing MTs. Direct monitoring
481 of MT-dependent transport of Crb and E-Cad during SG invagination will help clarify the
482 mechanism.

483 Upon knockdown of *crb* or *E-Cad,* less prominent apicomedial myosin web structures are
484 observed in invaginating SGs (Figure 8), suggesting a requirement of Crb and E-Cad in
485 proper organization of apical actomyosin networks during SG tube formation. Crb acts as
486 a negative regulator of actomyosin dynamics during *Drosophila* dorsal closure (Flores-
487 Benitez and Knust, 2015) and during SG invagination (Roper, 2012). It is possible that
488 proper Crb levels are required for modulating myosin activity both in the apicomedial
489 domain and at junctions during SG invagination, which contribute to apical constriction
490 and cell rearrangement, respectively (Roper, 2012; Sanchez-Corrales *et al.*, 2018).
491 Anisotropic localization of Crb and myosin was observed at the SG placode boundary,
492 where myosin accumulates at edges where Crb is lowest (Roper, 2012). Planar
493 polarization of Rok at this boundary is modulated through phosphorylation by Pak1
494 downstream of Crb (Sidor *et al.*, 2020). A further test will help understand whether and
495 how Crb might affect junctional myosin dynamics and SG invagination. As contractile
496 actomyosin structures exert forces on adherens junction to drive apical constriction, we
497 speculate that apical constriction defects upon *E-Cad* RNAi might be due to reduction of
498 cell adhesion and/or of improper force transmission. It will be interesting to determine if
499 the coordination of apical and junctional proteins and apical cytoskeletal networks through
500 intracellular trafficking is conserved during tubular organ formation in general.

501

502 **A role for dynein in apical constriction**

503 Dhc is also apically enriched in the dorsal/posterior region of the invaginating SG (Figure
504 1). Our data show that knockdown of *Dhc64C* not only affects Rok accumulation and
505 apicomedial myosin formation (Figure 5) but also disrupts MT organization in the SG
506 (Figure 3). This data is consistent with previous findings that cytoplasmic dynein is
507 associated with cellular structures and exerts tension on MTs. For example, dynein
508 tethered at the cell cortex can apply a pulling force on the MT network by walking towards
509 the minus end of a MT (Laan *et al.*, 2012). Dynein also scaffolds the apical cell cortex to
510 MTs to generate the forces that shape the tissue into a dome-like structure (Takeda *et*
511 *al.*, 2018). In interphase cells, the force generated by dynein also regulates MT turnover
512 and organization (Yvon *et al.*, 2001).

513 In *klar* mutants, on the other hand, MT organization is not affected in the SG (Figure 3),
514 suggesting that reduction of dynein-dependent trafficking by loss of *klar* does not cause
515 changes in the MT networks. Notably, although the intensity of apicomedial myosin does
516 not change upon *Dhc64C* knockdown or in the *klar* mutant background, formation of
517 apicomedial myosin web structures is affected (Figure 5). These data suggest a possible
518 scenario that dynein function is not required for myosin concentration in the apical domain
519 but is only needed for the spatial organization of apicomedial myosin. However, we
520 cannot rule out the possibility that the zygotic knockdown of *Dhc64C* by RNAi is not strong
521 enough to affect the intensity of apicomedial myosin. *Dhc64C* has strong maternal
522 expression and is essential for oogenesis and early embryo development (Li *et al.*, 1994).
523 Embryos with reduced maternal and zygotic pools of *Dhc64C* showed a range of
524 morphological defects in the entire embryo, some of which were severely distorted (data
525 not shown). Precise roles for dynein and dynein-dependent trafficking in regulating
526 apicomedial myosin formation remain to be elucidated.
527

528 **Materials and Methods**

529 **Fly stocks and husbandry**

530 Fly lines used in our experiments were listed in a separate table. All crosses were
531 performed at 25°C, unless stated otherwise.

532

533 **Antibody staining and confocal microscopy**

534 Antibodies used in our experiments were listed in a separate table. Embryos were
535 collected on grape juice-agar plates and processed for immunofluorescence using
536 standard procedures. Briefly, embryos were dechorionated in 50% bleach, fixed in 1:1
537 heptane:formaldehyde for 40 min and devitellinized with 80% EtOH, then stained with
538 primary and secondary antibodies in PBSTB (1X PBS, 0.1% Triton X-100, 0.2% BSA).
539 For acetylated α-tubulin, tyrosinated α-tubulin, sqh-GFP, Rok-GFP, Fog and phalloidin
540 staining, embryos were hand-devitellinized. All images were taken with a Leica SP8
541 confocal microscope.

542

543 **Cell segmentation and apical area quantification**

544 Embryos immunostained with E-Cad and CrebA were imaged using a Leica SP8 confocal
545 microscope. As Rok accumulation, apicomedial myosin and apical constriction depend
546 on the depth of invagination in the SG, SGs that were invaginated within the range of 5.1-
547 9.9 μm depth were used for quantification for proper comparison between different
548 genotypes. Maximum intensity projection was generated from three apical focal planes
549 with the highest E-Cad signals for all genotypes (0.3 μm apart for each focal plane). Cells
550 were segmented along E-Cad signals and cell areas were calculated using the Imaris
551 Program (Bitplane). Since the Imaris Program calculated the areas of both the front and
552 the back of the projected cell layer, we divided the measured areas by two to get the true
553 values of apical areas of SG cells.

554

555 **Negative correlation between apical area and Rab11/Nuf intensity**

556 Cell segmentation for five WT SGs within the range of 5.1- 9.9 μm invagination was
557 performed as described above. All experiments were carried out in the same condition,
558 and the same settings for confocal imaging were used. Three confocal sections in the

559 apical region that show the strongest Rab11/Nuf signals were used to produce the
560 maximum intensity projection. Intensity means were measured for Rab11/Nuf signals for
561 each segmented cell using the Imaris Program (Bitplane) and plotted. Correlation
562 (Pearson) and P values were calculated using the GraphPad Prism software.

563

564 **Total intensity of Rab11, Nuf and Fog signals**

565 For measuring the total intensity of Rab11/Nuf signals in the apical region of cells in the
566 whole SG placode, the integrated density of Rab11/Nuf of each SG cell was calculated
567 (integrated density= intensity mean x area). Intensity means and SG cell areas were
568 measured using the Imaris software. The total intensity was calculated as the sum of
569 integrated densities of all cells in the placode. Five SGs were used for quantification. P
570 values were calculated using Welch's t-test in the GraphPad Prism software.

571 For the total intensity of Fog signals, background corrections were carried out first. Using
572 the Fiji software, mean gray values of Fog signals of ten epidermal cells outside of the
573 SG placode were measured. The background intensity was calculated as the average
574 value of the intensity means of those ten cells. The intensity mean of Fog signals of all
575 SG cells was measured using the Imaris program, and the background intensity was
576 subtracted. After background correction, the intensity mean was multiplied by SG cell
577 areas to calculate the total Fog intensity. Five SGs were used for quantification. P values
578 were calculated using Welch's t-test in the GraphPad Prism software.

579

580 **The degree of variability for Rab11, Nuf, Fog and E-Cad signals**

581 The degree of variability of Rab11/Nuf signals was calculated as the ratio of deviation of
582 Rab11/Nuf intensity to the mean Rab11/Nuf intensity. The mean value of Rab11/Nuf
583 intensity was calculated as the average mean intensity of Rab11/Nuf signals in all SG
584 cells. Deviation of Rab11/Nuf intensity is the difference between the mean intensity of
585 Rab11/Nuf in each cell and the mean value. Five WT SGs (690 cells) and five spastin-

586 overexpressed SGs (496 cells) were analyzed and plotted. P values were calculated
587 using the Mann-Whitney U test in the GraphPad Prism software.

588 The degree of variability of Fog signals in control, spastin-overexpressing and Rab11
589 RNAi SGs was calculated using the same methods for Rab11/Nuf. Five SGs for each
590 genotype were analyzed (control (*fkh-Gal4/*+), 475 cells; *fkh-Gal4/UAS-Spastin*, 507
591 cells; *fkh-Gal4/UAS-Rab11* RNAi, 487 cells).

592 The degree of variability for E-Cad signals was calculated as the ratio of average deviation
593 of E-Cad to the mean E-Cad intensity. To measure the intensity of E-Cad signals along
594 the adherens junction, we drew a polyline along E-Cad signals at each junction. The
595 deviation and mean intensity of E-Cad signals were measured using the Leica LasX
596 software. SuperPlots (Lord *et al.*, 2020) were used to display the quantification. Each dot
597 in the graph represents the average value of 20 junctions in the dorsal posterior region of
598 each SG. Five SGs were analyzed for each genotype. P values were calculated using
599 Welch's t-test in the GraphPad Prism software.

600

601 **Quantification of intensities of myosin, Crb and E-Cad**

602 For myosin quantification, maximum intensity projections that span the apical and the
603 junctional region of SG cells were used (Leica LasX) and measurements were performed
604 using the Fiji software. Five SGs were used for quantification for each genotype. A group
605 of 20 cells in the dorsal/posterior region of the SG placode near the invagination pit was
606 selected for quantification of myosin intensity. Regions were drawn manually along the
607 inner or outer boundary of E-Cad signals of each cell to calculate the mean gray value of
608 apicomedial and junctional myosin.

609 For background correction, mean gray values of apicomedial myosin in ten cells outside
610 of the SG placode were measured. The average value of mean gray values of
611 apicomedial myosin in these ten cells was used to subtract the background of the cells
612 inside the placode from the same embryo. The mean intensity of apicomedial/junctional
613 myosin was normalized by the median deviation. SuperPlots (Lord *et al.*, 2020) were used

614 to display quantification. For myosin intensity, each dot in the graph represents the
615 average value of 20 cells in each SG. For Crb and E-Cad intensities, each dot in the graph
616 represents the average value of 10 cells for each SG. Five SGs were used for the
617 quantification of all three proteins. P values were calculated using Welch's t-test in the
618 GraphPad Prism software.

619

620 **Quantification of areas of Rok-GFP and apicomedial myosin puncta**

621 For quantification of area of Rok-GFP puncta, a single confocal section that had the
622 strongest medial Rok signals was selected. Cell boundaries were labeled by
623 immunostaining with the antibody against E-Cad. To analyze Rok distribution, we
624 performed Particle Analysis using the Fiji software. Fifteen cells in the dorsal/posterior
625 region near the invagination pit were selected for quantification. Rok-GFP signals were
626 converted into black-and-white using the *Threshold* tool in Photoshop before analysis.
627 Using the *Analyze particles* tool in Fiji, Rok-GFP puncta with areas equal or larger than
628 0.02 $\mu m^2$ were measured. Five SGs were used for quantification. P values were
629 calculated using Welch's t-test in the GraphPad Prism software.

630 For measuring areas of apicomedial myosin puncta, a single confocal section with the
631 strongest apicomedial myosin signals was selected. A group of 10 cells in the
632 dorsal/posterior region of SG was analyzed. Junctional myosin was excluded manually
633 and only apicomedial myosin signals were used for quantification. Measuring the area of
634 apicomedial myosin were carried out with the same method used for quantifying the area
635 of Rok-GFP puncta. Five SGs were used for quantification. P values were calculated
636 using Welch's t-test in the GraphPad Prism software.

637

638 **Quantification of length and number of gaps of junctional Crb**

639 Length of gaps and junctional length were measured using the Fiji software. Gaps that
640 have a length equal or more than 0.2 μm were quantified. If there were more than one

641 gap per junction, the length of gaps was calculated as a sum of all gaps in a given junction.
642 For each SG, ten cells in the dorsal/posterior region were used for quantification. For the
643 number of gaps, the total number of gaps in those ten cells was counted. Five SGs (~110
644 junctions) were used for quantification. P values were calculated using Welch's t-test in
645 the GraphPad Prism software.
646

647 **Table 1. List of fly lines used in this study.**

| Fly strains | Source | RRID | References |
|---|---|---|---|
| *Rab11-EYFP* | Bloomington Stock Center | 62549 | (Dunst *et al.*, 2015) |
| *Rab5-EYFP* | Bloomington Stock Center | 62543 | (Dunst *et al.*, 2015) |
| *Rab7-EYFP* | Bloomington Stock Center | 62545 | (Dunst *et al.*, 2015) |
| *UAS-Spastin* (on II) | N. Sherwood, Duke | | (Sherwood *et al.*, 2004) |
| *UAS-Spastin-CFP* (on III) | N. Sherwood, Duke | | (Du *et al.*, 2010) |
| *fkh-Gal4* (on II) | D. Andrew (John Hopkins University) | | (Chung *et al.*, 2017) |
| *fkh-Gal4* (on III) | D. Andrew (John Hopkins University) | | (Chung *et al.*, 2017) |
| *ubi-Rok-GFP* | S. Parkhurst (Fred Hutchinson Cancer Research Center) | | (Abreu-Blanco *et al.*, 2014) |
| *sqh-GFP* | | | (Royou *et al.*, 2004) |

| | | | |
|---|---|---|---|
| *UAS-Rab11S25N-EYFP* | Bloomington Stock Center | 9792, 23261 | |
| *UAS-Dicer-2* | Bloomington Stock Center | 60008 | |
| *UAS-Dhc64C* RNAi | Bloomington Stock Center<br><br>Vienna *Drosophila* Resource Center | 76941, 28749, v28053, v28054.<br><br>4 lines worked equally. V28054 was used for all of the data shown in this work. | |
| *Klar*$^{1}$ | Bloomington Stock Center | 3256 | |
| *klar*$^{mCD4}$ | Bloomington Stock Center | 25097 | |
| *klar*$^{mCD4}$ *ubi-Rok-GFP* | Recombinant line generated from *klar*$^{mCD4}$ and *ubi-Rok-GFP* | | |
| *UAS-Crb* RNAi | Bloomington Stock Center | 38373, 38903, 40869, 34999. | |

| | | | |
|---|---|---|---|
| | | 4 lines worked equally. 2 lines (38373, 34999) were used for the data shown in this work. | |
| *UAS-E-Cad* RNAi | Bloomington Stock Center | 32904 | |
| *UAS-Shg-GFP* | Bloomington Stock Center | 58445 | |
| *UAS-Rab11* RNAi | Bloomington Stock Center | 42709, 27730.<br><br>Line 42709 was used for testing myosin and Rok-GFP signals. Line 27730 was used for the rest of the experiments. | |

648

649 **Table 2. List of primary and secondary antibodies used in this study.**

| Antibody | Source | RRID | Dilution |
|---|---|---|---|
| α-E-Cad (rat) | DSHB (deposited by T. Uemura, Kyoto University) | DCAD2 (AB_528120) | 1:50 |
| α-CrebA (rat) | Andrew lab (John Hopkins University) | | 1:3000 |
| α-CrebA (rabbit) | Andrew lab (John Hopkins University) | | 1:5000 |
| α-Dhc (mouse) | DSHB (deposited by J.M. Scholey, University of California) | 2C11-2 (AB_2091523) | 1:50 |
| α-Rab11 (rabbit) | Andrew lab (John Hopkins University) | | 1:500 |
| α-Nuf (guinea pig) | Sotillos lab (CABD) | | 1:500 |
| α-acetylated α-tubulin (mouse) | Invitrogen | 32-2700 (AB_2533073) | 1:1000 |
| α-tyrosinated α-tubulin (rat) | Invitrogen | MA1-80017 (AB_2210201) | 1:1000 |
| α-GFP (chicken) | Invitrogen | A10262 (AB_2534023) | 1:500 |

| | | | |
|---|---|---|---|
| α-β-galactosidase (rabbit) | Invitrogen | A11132 (AB_221539) | 1:500 |
| α-Crb (mouse) | DSHB (deposited by E. Knust, Max Planck Institute) | Cq4 (AB_528181) | 1:10 |
| α-Fog (rabbit) | N. Fuse (Fuse et al., 2013) | | 1:1000 |
| α-Sec15 (guinea pig) | Bellen lab (Baylor College of Medicine) | | 1:2000 |
| Alexa Fluor 488/568/647-coupled secondary antibodies | Invitrogen | | 1:500 |

650

651 **Table 3. Genotypes in figure panels.**

| **Figures** | **Genotypes** |
|---|---|
| Figure 1B-F'''' | *Oregon R* |
| Figure 2A-B'', E-E' | *Oregon R* |
| Figure 2C-C''' | *fkh-Gal4/+* |
| Figure 2D-D''', F-F' | *fkh-Gal4/UAS-Spastin-CFP* |
| Figure 3A-A' | *fkh-Gal4/+* |
| Figure 3B-B' | *fkh-Gal4/UAS-Rab11-S25N-YFP* |
| Figure 3C-C' | *fkh-Gal4/UAS-Rab11* RNAi (TRiP.JF02812) |
| Figure 3D-D' | *UAS-Dicer-2/+; fkh-Gal4/UAS-Dhc64C* RNAi (GD12258) |
| Figure 3E-E' | *Oregon R* |
| Figure 3F-F' | *klar*$^{1}$ |
| Figure 3I-I'' | *UAS-Dicer-2/+; fkh-Gal4/+* |
| Figure 3J-J'' | *UAS-Dicer-2/+; fkh-Gal4/UAS-Dhc64C RNAi* (GD12258) |
| Figure 3K-K'' | *Oregon R* |
| Figure 3L-L'' | *klar*$^{mCD4}$ |
| Figure 4A-A'''' | *sqh-GFP/+; fkh-Gal4/+* |
| Figure 4B-B'''' | *sqh-GFP/UAS-Dicer-2; fkh-Gal4/UAS-Rab11* RNAi (UAS-Rab11.dsRNA.WIZ) |
| Figure 4F-F'' | *fkh-Gal4 ubi-Rok-GFP/+* |

| | |
|---|---|
| Figure 4G-G'' | *UAS-Dicer-2/+; fkh-Gal4 ubi-Rok-GFP/UAS-Rab11* RNAi (UAS-Rab11.dsRNA.WIZ) |
| Figure 5A-A'' | *sqh-GFP/+; fkhGal4/+* |
| Figure 5B-B'' | *sqh-GFP/UAS-Dicer-2; fkh-Gal4/UAS-Dhc64C* RNAi (GD12258) |
| Figure 5F-F'' | *sqh-GFP; sqh$^{AX3}$* |
| Figure 5G-G'' | *sqh-GFP; klar$^{1}$* |
| Figure 5K-K' | *fkh-Gal4 ubi-Rok-GFP/+* |
| Figure 5L-L' | *UAS-Spastin/+; fkh-Gal4 ubi-Rok-GFP/+* |
| Figure 5M-M' | *UAS-Dicer-2/+; fkh-Gal4 ubi-Rok-GFP/UAS-Dhc64C* RNAi (GD12258) |
| Figure 5N-N' | *ubi-Rok-GFP* |
| Figure 5O-O' | *klar$^{mCD4}$ ubi-Rok-GFP* |
| Figure 6A-A''', F-F'''' | *fkh-Gal4/+* |
| Figure 6B-B''', G-G'''' | *fkh-Gal4/UAS-Spastin* |
| Figure 6C-C''', H-H'''' | *fkh-Gal4/UAS-Rab11* RNAi (TRiP.JF02812) |
| Figure 7A-A' | *fkh-Gal4/+* |
| Figure 7B-B'' | *fkh-Gal4/UAS-Crb RNAi* (TRiP. HMS01409) |
| Figure 7C-C' | *fkh-Gal4/UAS-E-Cad* RNAi (TRiP.HMS00693) |
| Figure 8A-A'' | *sqh-GFP/+; fkh-Gal4/+* |

| | |
|---|---|
| Figure 8B-B'' | *sqh-GFP/+; fkh-Gal4/UAS-Crb* RNAi (TRiP.HMS01409) |
| Figure 8C-C'' | *sqh-GFP/+; fkh-Gal4/UAS-E-Cad* RNAi (TRiP.HMS00693) |
| Figure 8D-D'' | *fkh-Gal4 ubi-Rok-GFP/+* |
| Figure 8E-E'' | *fkh-Gal4 ubi-Rok-GFP/UAS-Crb* RNAi (TRiP.HMS01409) |
| Figure 8F-F'' | *fkh-Gal4 ubi-Rok-GFP/UAS-E-Cad* RNAi (TRiP.HMS00693) |
| Figure S1A-A''''' | *Rab11-EYFP* |
| Figure S1B-B''' | *Rab5-EYFP* |
| Figure S1D-D''' | *Rab7-EYFP* |
| Figure S1E-E''' | *Oregon R* |
| Figure S2A-A'', C-C' | *fkh-Gal4/+* |
| Figure S2B-B'', D-D' | *fkh-Gal4/UAS-Spastin-CFP* |
| Figure S3A-A', B-B', E, F | *fkh-Gal4/+* |
| Figure S3C-C', D-D' | *fkh-Gal4/UAS-Rab11* RNAi (TRiP.JF02812) |
| Figure S3E' | *fkh-Gal4/UAS-Crb* RNAi (TRiP.HMS01409) |
| Figure S3F' | *fkh-Gal4/UAS-E-Cad* RNAi (TRiP.HMS00693) |
| Figure S4A-A''', C-C'' | *fkh-Gal4/+* |
| Figure S4B-B''', D-D'' | *fkh-Gal4/UAS-Spastin* |
| Figure S4E-E'' | *fkh-Gal4/UAS-Rab11* RNAi (TRiP.JF02812) |

| | |
|---|---|
| Figure S4F-F’’’ | *UAS-Crb/+; fkh-Gal4/+* |
| Figure S4G-G’’’ | *UAS-Crb/+; fkh-Gal4/UAS-Spastin* |
| Figure S4H-H’’’ | *fkh-Gal4/UAS-Shg-GFP* |
| Figure S4I-I’’’ | *UAS-Spastin/+; fkh-Gal4/UAS-Shg-GFP* |

652

653

## Acknowledgments

We thank the members of the Chung laboratory for comments and suggestions. We thank A. Martin, S. Parkhurst and N. Sherwood and the Bloomington stock center for fly stocks, and D. Andrew, H. Bellen, S. Sotillos and the Developmental Studies Hybridoma Bank for antibodies. We thank Flybase for the gene information. We are grateful to A. Bohnert, C. Hanlon, A. Johnson and C. O'Kane for their helpful comments on the manuscript. This work is supported by start-up fund from Louisiana State University and the grant from the Board of Regents Research Competitiveness Subprogram GR-00005224 to S.C.

663 **Figure legends**

664

665 **Figure 1. Intracellular trafficking components are apically enriched in invaginating**
666 **SGs.** (A) A schematic drawing of the anterior region of the *Drosophila* embryo for stage
667 11 (ventral and lateral views) and stage 16 (lateral view) with SGs shown in green. Top
668 right, magnified view of a stage 11 SG. The region where SG cells undergo clustered
669 apical constriction during invagination is shown in purple. (B-B'') En face (top) and lateral
670 (bottom) views of a wild type stage 11 SG immunostained for E-Cad, Rab11 and Nuf.
671 Rab11 and Nuf show apical enrichment near the invagination pit (yellow arrowheads).
672 Red arrowheads, Rab11 and Nuf signals near the segmental groove. (B'''-B''''') Heat
673 maps of apical area (B''') and intensity of Rab11 (B'''') and Nuf (B''''). Cells with smaller
674 apical areas near the invagination pit (dark blue cells in B''') show the high intensity of
675 Rab11 and Nuf (red signals in B'''' and B''''). (C-C''') En face (top) and lateral (bottom)
676 views of a wild type stage 11 SG immunostained for E-Cad (C) and Dhc64C (C').
677 Corresponding heat maps for apical areas (C'') and intensity of Dhc64C signals (C''') are
678 shown. (D-F''') Wild type stage 11 SGs immunostained for E-Cad and Rab11 at different
679 timepoints of invagination. (G) The total intensity of Rab11 in the whole SG placode before
680 and during invagination. Before invagination, n= 4 SGs; during invagination, n= 5 SGs.
681 (H) Negative correlation between Rab11 intensities and apical areas of SG cells before
682 (top) and during invagination (bottom). R, Pearson correlation coefficient. $P < 0.0001$ for
683 all samples. Before invagination, n= 4 SGs, 506 cells; during invagination, n= 4 SGs, 561
684 cells. Asterisks: invagination pit. White lines: SG boundary. SG boundaries are marked
685 based on CrebA (SG nuclear marker) signals in the basal region of SG cells (not shown).

686

Figure 1

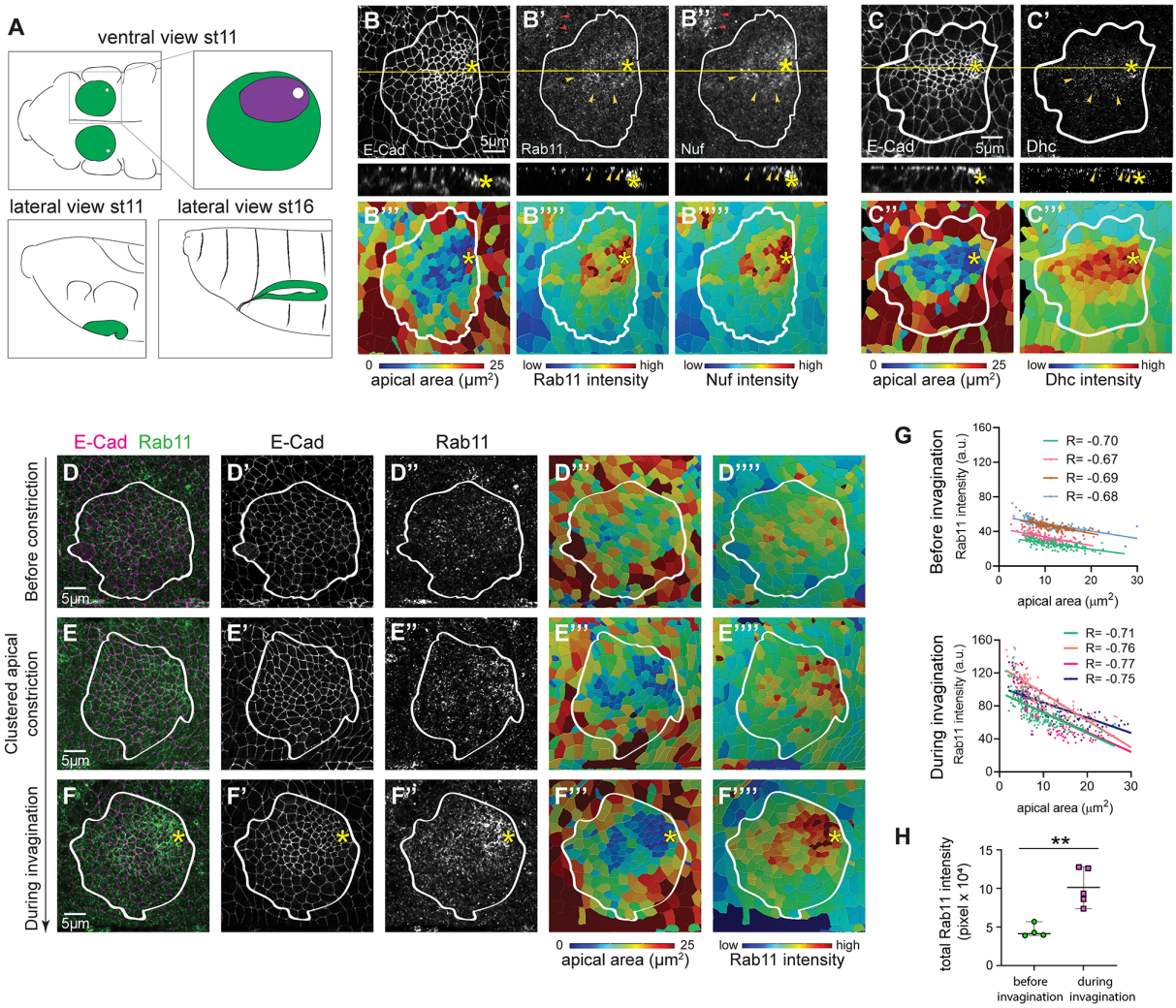
A
ventral view st11
lateral view st11
lateral view st16
B
B'
B''
C
C'
E-Cad
Rab11
Nuf
Dhc
5µm
B'''
B''''
B'''''
C''
C'''
0
25
apical area (µm²)
low
high
Rab11 intensity
Nuf intensity
Dhc intensity
E-Cad Rab11
E-Cad
Rab11
Before constriction
Clustered apical constriction
During invagination
D
D'
D''
D'''
D''''
E
E'
E''
E'''
E''''
F
F'
F''
F'''
F''''
G
Before invagination
Rab11 intensity (a.u.)
R= -0.70
R= -0.67
R= -0.69
R= -0.68
apical area (µm²)
During invagination
R= -0.71
R= -0.76
R= -0.77
R= -0.75
H
total Rab11 intensity (pixel x 10⁴)
**
before invagination
during invagination

687

688 **Figure 2. Disruption of MTs results in mislocalization of Rab11 and Nuf to the**
689 **basolateral domain in SG cells.** (A-A'''') A wild type SG immunostained for Rab11
690 (green) and tyrosinated α-tubulin (Tyr-α-Tub; purple). Higher magnification of the yellow
691 boxed area is shown in A'-A'''. Yellow arrowheads, co-localized Rab11 and tyrosinated
692 α-tubulin. (B-B'') Z sections along the yellow line in A. (C-C''') En face (top) and lateral
693 (bottom) views of a control (*fkh-Gal4/*+) SG show abundant levels of tyrosinated α-tubulin
694 (C''; Tyr-α-Tub) and acetylated α-tubulin (C'''; Ace-α-Tub). (D-D''') Overexpression of
695 spastin in the SG using *fkh-Gal4* leads to a reduction of tyrosinated α-tubulin (D'') and
696 loss of acetylated α-tubulin (D'''). Whereas Rab11 is enriched in the apical domain of WT
697 SG cells (yellow arrowheads in C'), Rab11 mislocalizes basolaterally when spastin is
698 overexpressed (red arrowheads in D'). (E-F'') Confocal images of WT (E and E') and
699 spastin-overexpressing SGs (F, F') stained for Rab11 (E, F) and Nuf (E', F'). The
700 maximum projection of three confocal sections for the apical domain is shown. Compared
701 to strong Rab11 and Nuf signals in the apical domain in WT SGs (yellow arrowheads in
702 E and E'), Rab11 and Nuf are reduced in spastin-overexpressing SGs (red arrowheads
703 in F and F'). (G) The total intensity of Rab11 and Nuf in the whole SG placode in control
704 and spastin-overexpressing SG. n= 5 SGs for each genotype. (H) The degree of variability
705 of Rab11 (left) and Nuf (right) intensities in the SG (n= 5 SGs for both genotypes; WT,
706 690 cells; *fkh-Gal4/UAS-Spastin*, 496 cells). ****, $p<0.0001$, Mann-Whitney U test.
707 Asterisks: invagination pit. White lines: SG boundary.

Figure 2

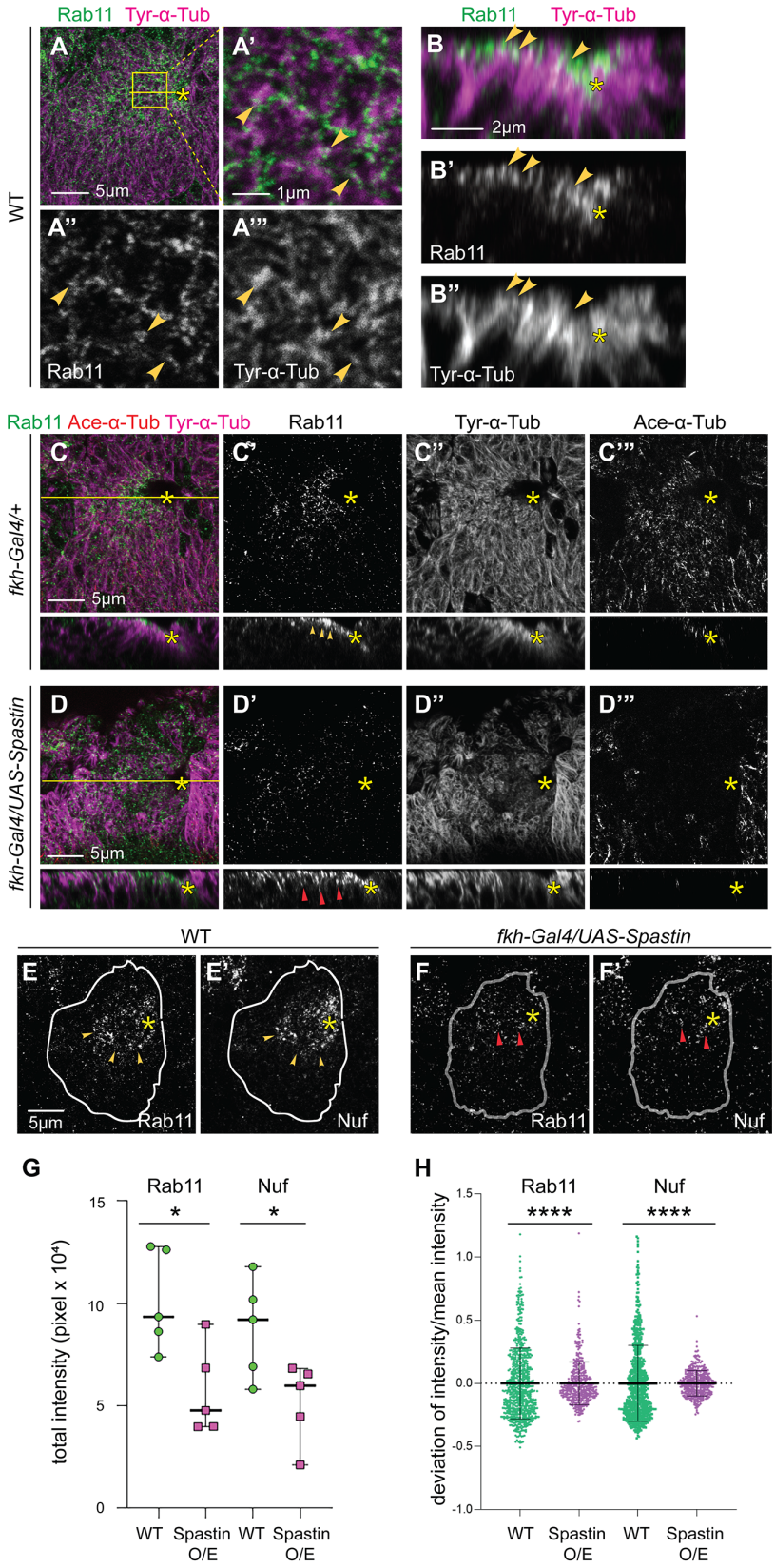
Rab11 Tyr-α-Tub
A
A'
A''
A'''
WT
5μm
1μm
Rab11
Tyr-α-Tub
B
B'
B''
2μm
Rab11 Ace-α-Tub Tyr-α-Tub
Rab11
Tyr-α-Tub
Ace-α-Tub
C
C'
C''
C'''
fkh-Gal4/+
D
D'
D''
D'''
fkh-Gal4/UAS-Spastin
WT
fkh-Gal4/UAS-Spastin
E
E'
F
F'
Nuf
G
H
total intensity (pixel x 10⁴)
deviation of intensity/mean intensity
WT
Spastin O/E

708

709 **Figure 3. Rab11 and dynein functions are required for coordinated apical**
710 **constriction in the SG.** (A-F) Confocal images of control (A), Rab11-DN-overexpressing
711 (B), *Rab11* RNAi (C), *Dhc64C* RNAi (D), wild type (E) and *klar* mutant (F) SGs
712 immunostained for E-Cad. (A'-F') Heat maps corresponding to images shown in A-F. (G,
713 H) Percentage (G) and cumulative percentage (H) of SG cells with different apical areas.
714 Mann-Whitney U test (for the percentage of cells) and Kolmogorov-Smirnov test (for the
715 cumulative percentage of cells). N= 5 SGs (control (*fkh-Gal4/*+), 517 cells; *fkh>Rab11-*
716 *DN*, 536 cells; *fkh>Rab11* RNAi, 474 cells; *fkh>Dhc64C* RNAi, 499 cells) and 6 SGs (WT,
717 690 cells; $klar^{1}$, 705 cells). *, $p<0.05$; ****, $p<0.0001$. (I-J'') Control (I-I'') and *Dhc64C* RNAi
718 (J-J'') SGs stained for tyrosinated-α-Tub (I', J') and phalloidin (I'', J''). Compared to control
719 (I'), tyrosinated-α-Tub (Tyr-α-Tub) is decreased in *Dhc64C* RNAi SGs (J'). (I-J'') WT (K-
720 K'') and *klar* mutant (L-L'') SGs stained for acetylated-α-Tub (Ace-α-Tub; K', K') and
721 phalloidin (L'', L''). No significant changes in acetylated-α-Tub levels are detected in *klar*
722 mutant SGs. Asterisks: invagination pit. White lines: SG boundary.

Figure 3

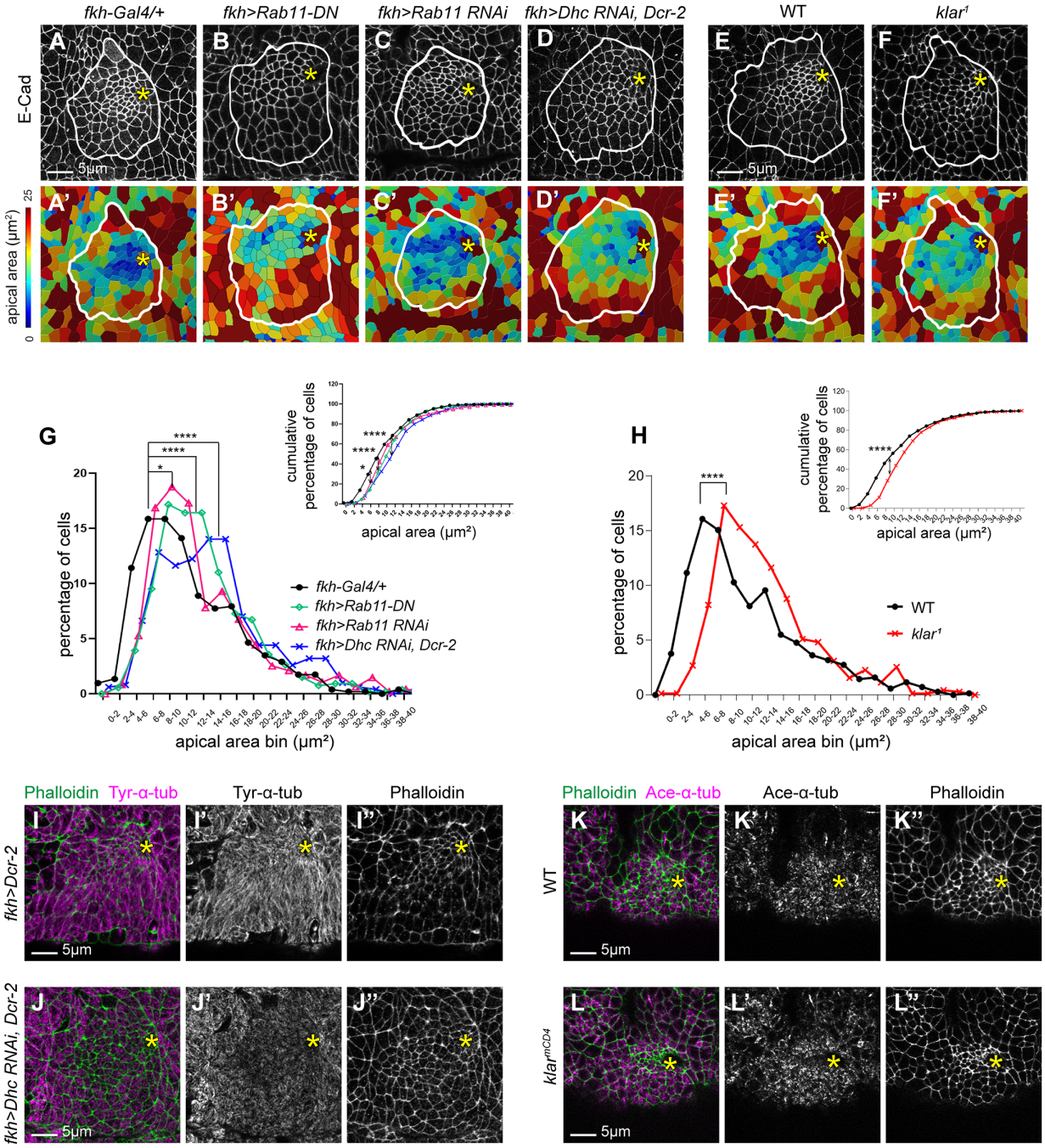


723

724

725 **Figure 4. Compromised Rab11 functions lead to a reduction of apicomedial myosin**
726 **formation and impair apicomedial Rok accumulation in SG cells.** (A-B’’’) sqh-GFP
727 signals in control (A-A’’’) and *Rab11* RNAi (B-B’’’) SGs immunostained for E-Cad and
728 GFP. Higher magnification of the yellow boxed area in A and B are shown in A’’-A’’’ and
729 B’’-B’’’. Compared to strong signals of apicomedial myosin web structures in the control
730 SG (yellow arrowheads in A’’), reduced and dispersed myosin signals are detected upon
731 *Rab11* knockdown (red arrowheads in B’’). (A’’’’ and B’’’’) Inverted sqh-GFP signals are
732 used for measuring areas of apicomedial myosin structures. (C-E) Quantification of the
733 intensity of apicomedial (AM) and junctional (J) myosin I, the ratio of apicomedial to
734 junctional myosin (D) and areas of apicomedial myosin (E) in control and *Rab11* RNAi
735 SG cells. n= 5 SGs for both genotypes; 10 cells in the dorsal/posterior region of each SG.
736 *, $p< 0.05$; **, $p< 0.01$. Welch’s t-test. (F-G’’) Rok-GFP signals in control (F, F’) and Rab11
737 RNAi (G, G’) SGs immunostained for E-Cad and GFP. Higher magnification of the yellow
738 boxed area in F and G are shown in F’ and G’. Compared to the strong accumulation of
739 Rok-GFP signals in the apicomedial region of control SG cells (yellow arrowheads in F’),
740 Rok-GFP signals are more dispersed when *Rab11* is knocked down (red arrowheads in
741 G’). (F’’ and G’’) Inverted Rok-GFP signals are used for measuring areas of apicomedial
742 Rok accumulation. (H) Quantification of areas of Rok-GFP puncta. *, $p< 0.05$; **, $p<0.01$.
743 Welch’s t-test. n= 5 SGs for all genotypes; 15 cells in the dorsal/posterior region for each
744 SG. Asterisks: invagination pit.

Figure 4

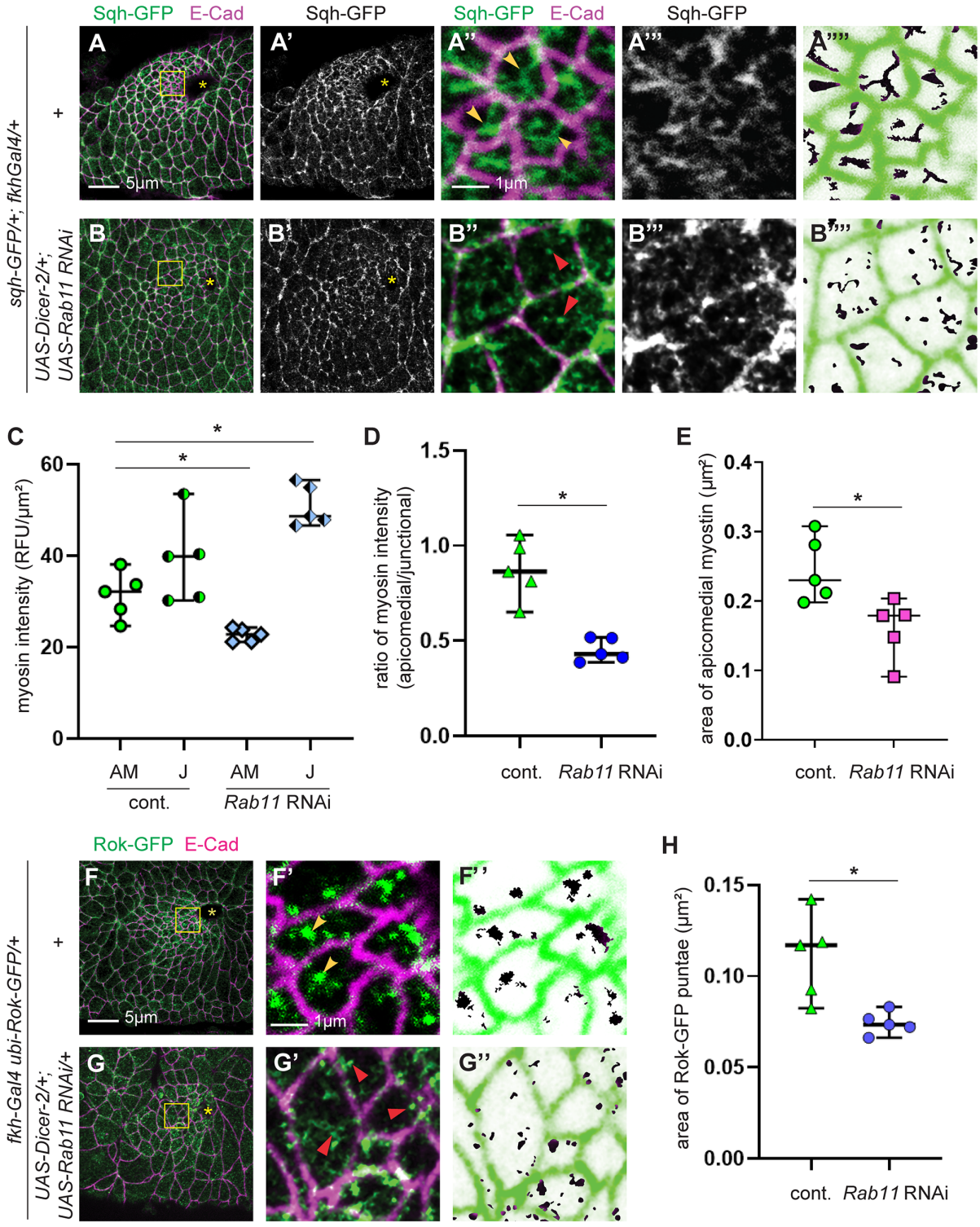
Sqh-GFP E-Cad
Sqh-GFP
Sqh-GFP E-Cad
Sqh-GFP
A
A'
A''
A'''
A''''
B
B'
B''
B'''
B''''
5µm
1µm
sqh-GFP/+; fkhGal4/+
+
UAS-Dicer-2/+;
UAS-Rab11 RNAi
C
myosin intensity (RFU/µm²)
AM
J
cont.
Rab11 RNAi
D
ratio of myosin intensity (apicomedial/junctional)
cont.
Rab11 RNAi
E
area of apicomedial myostin (µm²)
cont.
Rab11 RNAi
Rok-GFP E-Cad
F
F'
F''
G
G'
G''
fkh-Gal4 ubi-Rok-GFP/+
UAS-Dicer-2/+;
UAS-Rab11 RNAi/+
H
area of Rok-GFP puntae (µm²)
cont.
Rab11 RNAi

745

746 **Figure 5. Compromised dynein function leads to a reduction of apicomedial myosin**
747 **formation and impairs apicomedial Rok accumulation in SG cells.** (A-B'', F-G'') sqh-
748 GFP signals in control (A-A'', F-F''), *Dhc64C* RNAi (B-B'') and *klar* mutant (G-G'') SGs
749 immunostained for E-Cad and GFP. Higher magnification of the yellow boxed area in A,
750 B, F and G are shown in A', A'', B', B'', F', F'', G' and G'. Yellow and red arrowheads
751 indicate apicomedial myosin. (C-E, H-J) Quantification of the intensity of apicomedial and
752 junctional myosin (C, H), the ratio of apicomedial to junctional myosin (D, I) and areas of
753 apicomedial myosin (E, J) in SG cells. n= 5 SGs for all genotypes; 10 cells in the
754 dorsal/posterior region of each SG. *, $p< 0.05$; **, $p< 0.01$, Welch's t-test. (A-A'') (K-O')
755 Rok-GFP signals in control (K, K', N, N'), spastin-overexpressing (L, L'), *Dhc64C* RNAi
756 (M, M') and *klar* mutant (O, O') SGs immunostained for E-Cad and GFP. Higher
757 magnification of the yellow boxed area in K-O are shown in K'-O'. (P, Q) Quantification of
758 areas of Rok-GFP puncta. *, $p< 0.05$; **, $P<0.01$, Welch's t-test. n= 5 SGs for all
759 genotypes; 15 cells in the dorsal/posterior region for each SG. Asterisks: invagination pit.

Figure 5

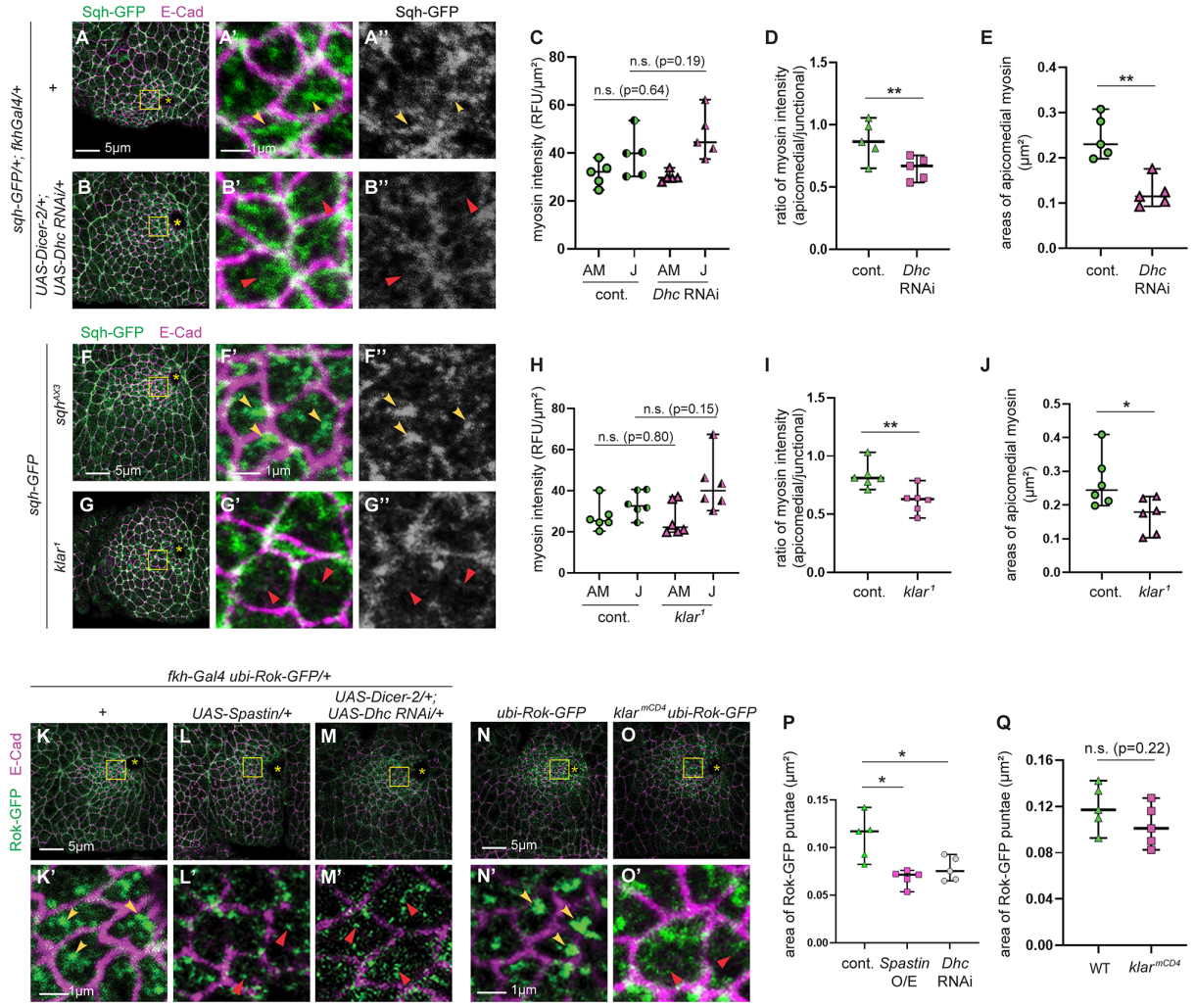
Sqh-GFP E-Cad
Sqh-GFP
sqh-GFP/+; fkhGal4/+
+
UAS-Dicer-2/+; UAS-Dhc RNAi/+
5µm
1µm
myosin intensity (RFU/µm²)
n.s. (p=0.19)
n.s. (p=0.64)
AM J AM J
cont. Dhc RNAi
ratio of myosin intensity (apicomedial/junctional)
areas of apicomedial myosin (µm²)
sqh-GFP
sqhX3
klar1
n.s. (p=0.15)
n.s. (p=0.80)
fkh-Gal4 ubi-Rok-GFP/+
UAS-Spastin/+
ubi-Rok-GFP
klarmCD4 ubi-Rok-GFP
E-Cad
Rok-GFP
area of Rok-GFP puntae (µm²)
cont. Spastin O/E Dhc RNAi
WT klarmCD4

762 **Figure 6. MTs and Rab11 are required for apical transport of Fog, Crb and E-Cad**
763 **during SG invagination.** (A-C') Confocal images for control (A-A'), spastin-
764 overexpressing (B-B') and *Rab11* RNAi (C-C') SGs immunostained for E-Cad and Fog.
765 (A''-C''') Corresponding heat maps for apical areas (A''-C'') and Fog intensity (A'''-C''').
766 (D) Total intensity of apical Fog signals in the entire SG placode in control, spastin-
767 overexpressing and *Rab11* knocked down SG. n= 5 SGs for each genotype. (E) The
768 degree of variability for Fog signals. n= 5 SGs (control (*fkh-Gal4/*+), 475 cells; *fkh-*
769 *Gal4/UAS-spastin*, 507 cells; *fkh-Gal4/UAS-Rab11* RNAi, 487 cells). Kolmogorov-
770 Smirnov test. (F-H'''') Confocal images for control (F-F''''), spastin-overexpressing (G-
771 G'''') and *Rab11* RNAi (H-H'''') SGs immunostained for E-Cad and Crb. Higher
772 magnification of boxed areas in F-H are shown in F'''-H''''. Compared to relatively
773 continuous Crb signals in the control SG (F'''), Crb signals show gaps (red arrows) in
774 spastin-overexpressing (G''') and *Rab11* RNAi (H''') SGs. Compared to relatively uniform
775 E-Cad signals along adherens junctions in the control SG (F''''), E-Cad signals in spastin-
776 overexpressing (G'''') and *Rab11* RNAi (H'''') SGs are unevenly distributed. Yellow boxes,
777 representative junctions. (I) Quantification of the ratio of length of gaps to junctional length
778 (Welch's t-test) in SGs immunostained for Crb. (J) Quantification of the number of gaps
779 (Welch's t-test) in SGs immunostained for Crb. n= 5 SGs; 10 cells for each SG. (K) The
780 degree of variability of E-Cad intensities in the SG. n= 5 SGs; 20 junctions for each SG.
781 Welch's t-test. *, $p<0.05$; **, $p< 0.01$; ****, $p< 0.0001$. Asterisks: invagination pit. White
782 lines: SG boundary.

FIgure 6

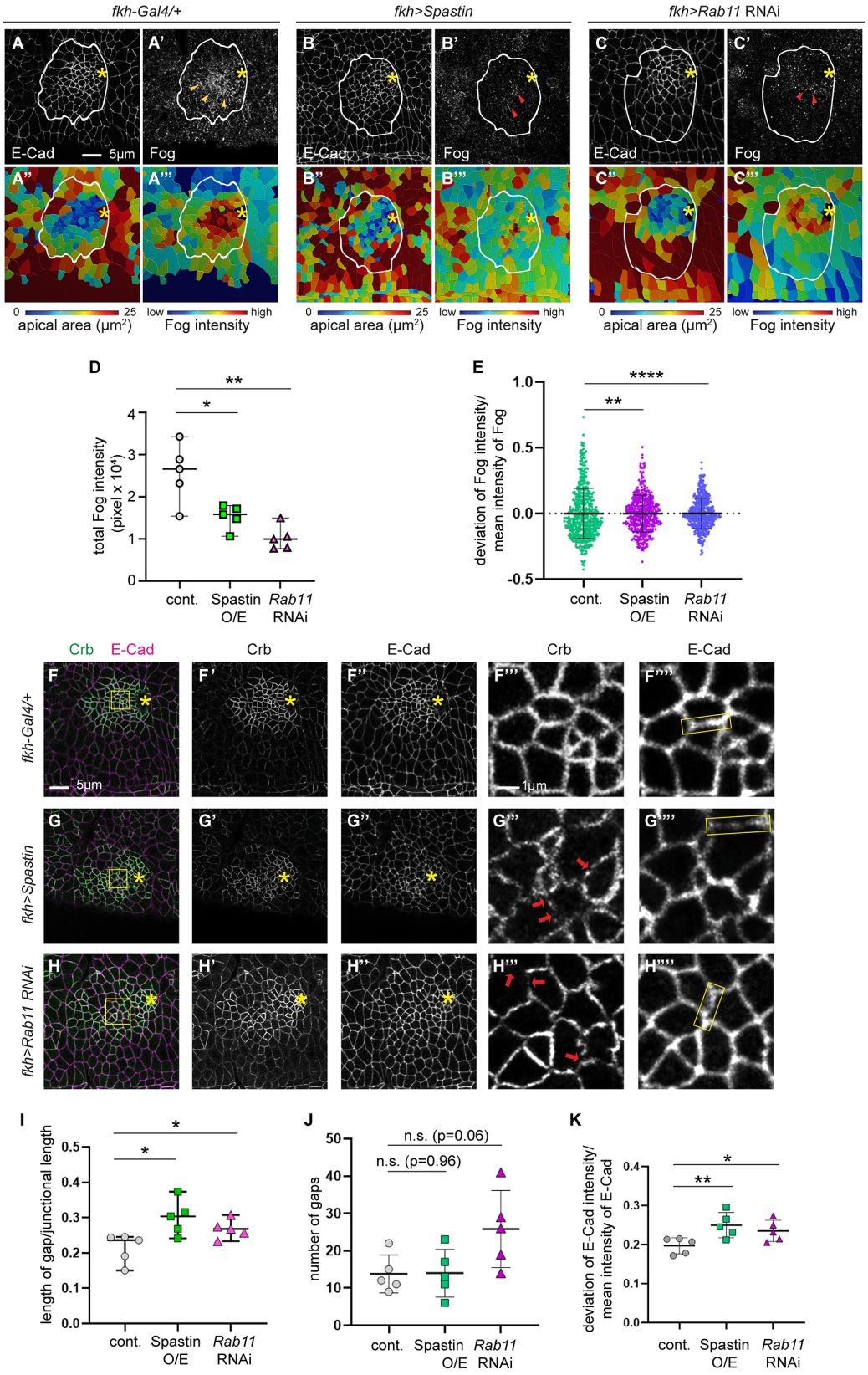
fkh-Gal4/+
fkh>Spastin
fkh>Rab11 RNAi
A
A'
B
B'
C
C'
E-Cad
5μm
Fog
A''
A'''
B''
B'''
C''
C'''
0
25
apical area (μm²)
low
high
Fog intensity
D
total Fog intensity (pixel x 10⁴)
cont.
Spastin O/E
Rab11 RNAi
E
deviation of Fog intensity/ mean intensity of Fog
Crb
E-Cad
F
F'
F''
F'''
F''''
G
G'
G''
G'''
G''''
H
H'
H''
H'''
H''''
1μm
fkh-Gal4/+
fkh>Spastin
fkh>Rab11 RNAi
I
length of gap/junctional length
J
number of gaps
n.s. (p=0.06)
n.s. (p=0.96)
K
deviation of E-Cad intensity/ mean intensity of E-Cad

783

784 **Figure 7. Crb and E-Cad have roles in regulating apical constriction during SG**
785 **invagination.** (A-C) Confocal images of control (A), *crb* RNAi (B) and *E-Cad* RNAi (C)
786 SGs immunostained for E-Cad. (A'-C') Corresponding heat maps for apical areas in SGs
787 in A-C. (D) Percentage and cumulative percentage of cells with different apical areas.
788 Mann-Whitney U test (percentage of cells) and Kolmogorov-Smirnov test (cumulative
789 percentage of cells). n= 5 SGs (control, 517 cells; *crb* RNAi, 583 cells; *E-Cad* RNAi, 712
790 cells). *, $p<0.05$; ****, $p<0.0001$. Asterisks: invagination pit. White lines: SG boundary.

Figure 7

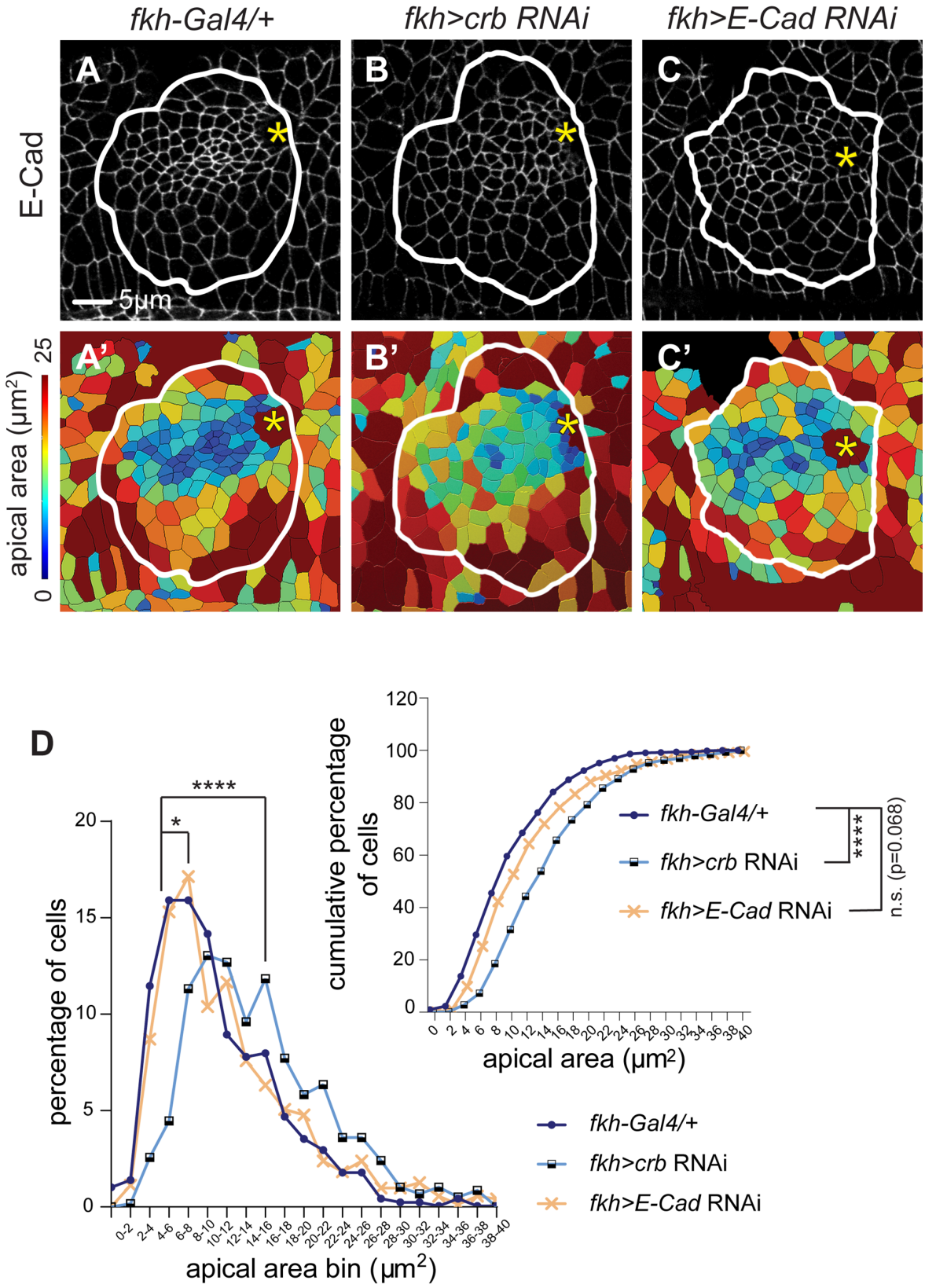
fkh-Gal4/+
fkh>crb RNAi
fkh>E-Cad RNAi
A
B
C
E-Cad
5µm
A'
B'
C'
apical area (µm²)
25
0
D
****
*
percentage of cells
apical area bin (µm²)
cumulative percentage of cells
apical area (µm²)
fkh-Gal4/+
fkh>crb RNAi
fkh>E-Cad RNAi
****
n.s. (p=0.068)

791

**Figure 8. Knockdown of *crb* or *E-Cad* results in reduced apicomedial myosin formation and dispersed apicomedial Rok.** (A-C") sqh-GFP signals in control (A-A''), *crb* RNAi (B-B'') and *E-Cad* RNAi (C-C'') SGs immunostained for E-Cad and GFP. (A"-C") Higher magnification of yellow boxed areas in A-C. (D-F") Rok-GFP signals in control (D-D''), *crb* RNAi (E-E'') and *E-Cad* RNAi (F-F'') SGs immunostained for E-Cad and GFP. (D"-F") Higher magnification of yellow boxed areas in D-F. (G-I) Quantification of the intensity of apicomedial and junctional myosin (G), the ratio of apicomedial to junctional myosin (H) and areas of apicomedial myosin structures (I) in SG cells from different genotypes shown in A-C (n=5 SGs for each genotype; 10 cells in the dorsal/ posterior region). *, p<0.05; **, p<0.01. Welch's t-test. (F-I'') (J) Quantification of areas of Rok-GFP puncta in SG cells from different genotypes shown in D-F (n=5 SGs; 15 cells in the dorsal/posterior for each genotype). *, p<0.05; **, p< 0.01. Welch's t-test. Asterisks: invagination pit.

Figure 8

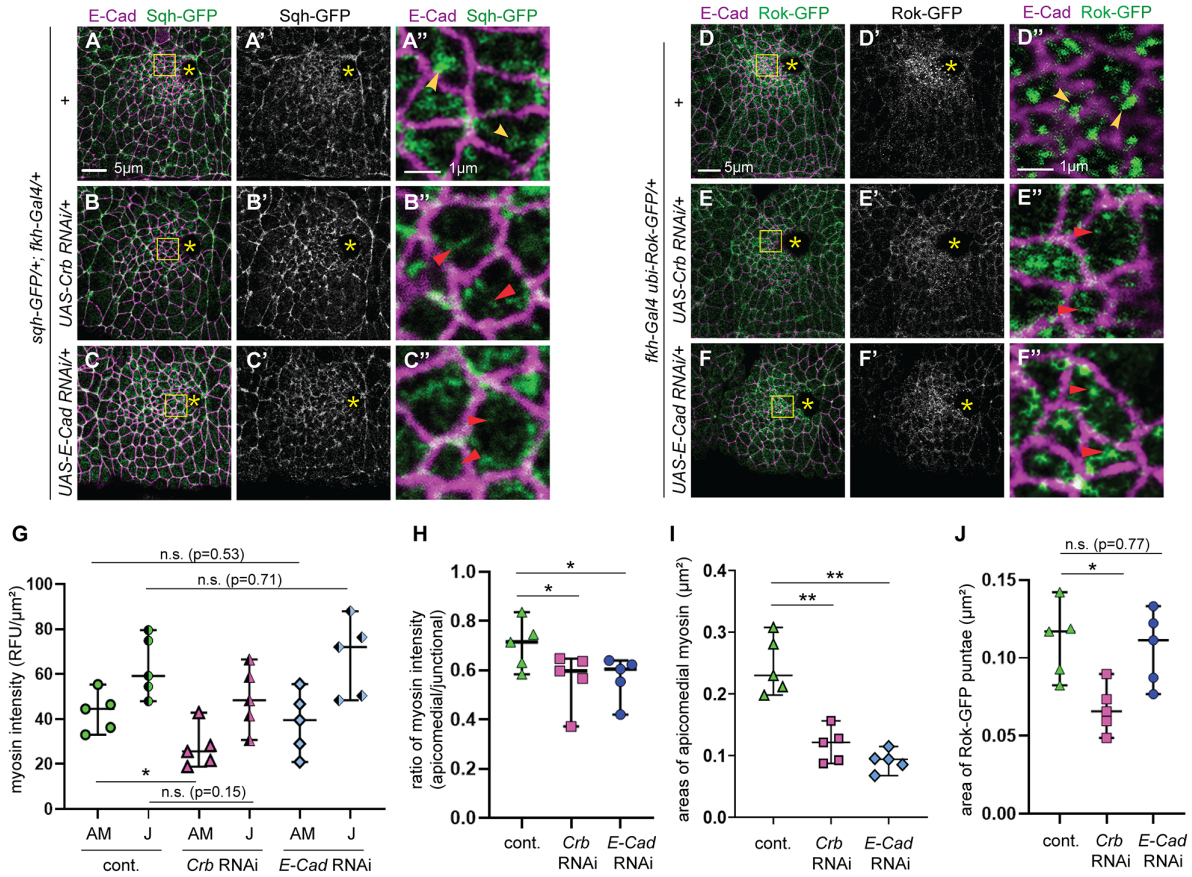

806 **Figure 9. A proposed model for MT-dependent trafficking to promote apical**
807 **constriction during SG invagination.** Vesicular transport is essential for apical
808 localization of Fog, Crb and E-Cad to regulate apical myosin networks and subsequent
809 apical constriction. Precise roles for the dynein motor in regulating apical constriction
810 remain to be determined. The red question mark represents a potential role of dynein in
811 trafficking cargos to the apical region of SG cells during apical constriction.

Figure 9

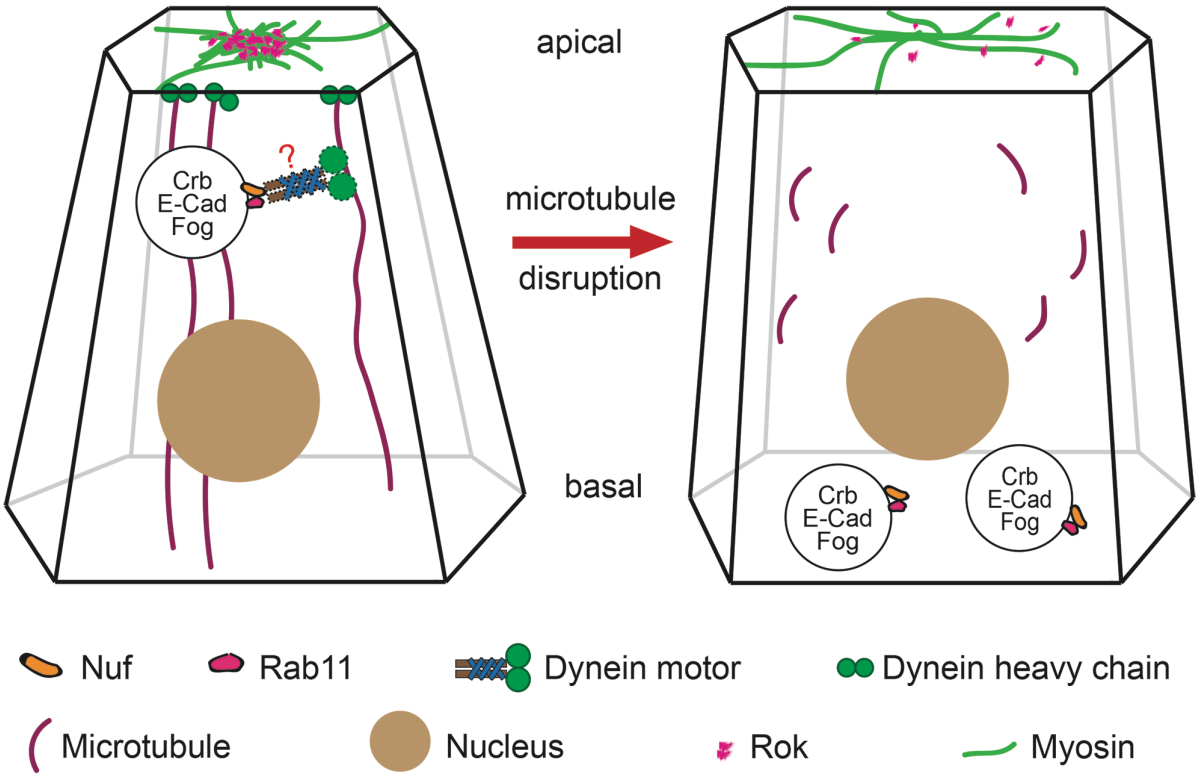


812
813

814 ## References


815 Abreu-Blanco, M.T., Verboon, J.M., and Parkhurst, S.M. (2014). Coordination of Rho family GTPase
816 activities to orchestrate cytoskeleton responses during cell wound repair. Curr Biol *24*, 144-155.
817 Aguilar-Aragon, M., Fletcher, G., and Thompson, B.J. (2020). The cytoskeletal motor proteins Dynein and
818 MyoV direct apical transport of Crumbs. Dev Biol *459*, 126-137.
819 Anborgh, P.H., Seachrist, J.L., Dale, L.B., and Ferguson, S.S. (2000). Receptor/beta-arrestin complex
820 formation and the differential trafficking and resensitization of beta2-adrenergic and angiotensin II type
821 1A receptors. Mol Endocrinol *14*, 2040-2053.
822 Andrew, D.J., and Ewald, A.J. (2010). Morphogenesis of epithelial tubes: Insights into tube formation,
823 elongation, and elaboration. Dev Biol *341*, 34-55.
824 Benton, M.A., Frey, N., Nunes da Fonseca, R., von Levetzow, C., Stappert, D., Hakeemi, M.S., Conrads,
825 K.H., Pechmann, M., Panfilio, K.A., Lynch, J.A., and Roth, S. (2019). Fog signaling has diverse roles in
826 epithelial morphogenesis in insects. Elife *8*.
827 Booth, A.J.R., Blanchard, G.B., Adams, R.J., and Roper, K. (2014). A dynamic microtubule cytoskeleton
828 directs medial actomyosin function during tube formation. Dev Cell *29*, 562-576.
829 Burbank, K.S., Groen, A.C., Perlman, Z.E., Fisher, D.S., and Mitchison, T.J. (2006). A new method reveals
830 microtubule minus ends throughout the meiotic spindle. J Cell Biol *175*, 369-375.
831 Cerniello, F.M., Carretero, O.A., Longo Carbajosa, N.A., Cerrato, B.D., Santos, R.A., Grecco, H.E., and
832 Gironacci, M.M. (2017). MAS1 Receptor Trafficking Involves ERK1/2 Activation Through a beta-Arrestin2-
833 Dependent Pathway. Hypertension *70*, 982-989.
834 Chung, S., and Andrew, D.J. (2014). Cadherin 99C regulates apical expansion and cell rearrangement
835 during epithelial tube elongation. Development *141*, 1950-1960.
836 Chung, S., Hanlon, C.D., and Andrew, D.J. (2014). Building and specializing epithelial tubular organs: the
837 Drosophila salivary gland as a model system for revealing how epithelial organs are specified, form and
838 specialize. Wiley Interdiscip Rev Dev Biol *3*, 281-300.
839 Chung, S., Kim, S., and Andrew, D.J. (2017). Uncoupling apical constriction from tissue invagination. Elife
840 *6*.
841 Dale, L.B., Seachrist, J.L., Babwah, A.V., and Ferguson, S.S. (2004). Regulation of angiotensin II type 1A
842 receptor intracellular retention, degradation, and recycling by Rab5, Rab7, and Rab11 GTPases. J Biol
843 Chem *279*, 13110-13118.
844 David, D.J., Tishkina, A., and Harris, T.J. (2010). The PAR complex regulates pulsed actomyosin
845 contractions during amnioserosa apical constriction in Drosophila. Development *137*, 1645-1655.
846 Du, F., Ozdowski, E.F., Kotowski, I.K., Marchuk, D.A., and Sherwood, N.T. (2010). Functional conservation
847 of human Spastin in a Drosophila model of autosomal dominant-hereditary spastic paraplegia. Hum Mol
848 Genet *19*, 1883-1896.
849 Dunst, S., Kazimiers, T., von Zadow, F., Jambor, H., Sagner, A., Brankatschk, B., Mahmoud, A., Spannl, S.,
850 Tomancak, P., Eaton, S., and Brankatschk, M. (2015). Endogenously tagged rab proteins: a resource to
851 study membrane trafficking in Drosophila. Dev Cell *33*, 351-365.
852 Elting, M.W., Hueschen, C.L., Udy, D.B., and Dumont, S. (2014). Force on spindle microtubule minus ends
853 moves chromosomes. J Cell Biol *206*, 245-256.
854 Fan, G.H., Lapierre, L.A., Goldenring, J.R., and Richmond, A. (2003). Differential regulation of CXCR2
855 trafficking by Rab GTPases. Blood *101*, 2115-2124.
856 Flores-Benitez, D., and Knust, E. (2015). Crumbs is an essential regulator of cytoskeletal dynamics and
857 cell-cell adhesion during dorsal closure in Drosophila. Elife *4*.
858 Gorvel, J.P., Chavrier, P., Zerial, M., and Gruenberg, J. (1991). rab5 controls early endosome fusion in
859 vitro. Cell *64*, 915-925.

860 Goshima, G., Nedelec, F., and Vale, R.D. (2005). Mechanisms for focusing mitotic spindle poles by minus
861 end-directed motor proteins. J Cell Biol *171*, 229-240.
862 Gross, S.P., Welte, M.A., Block, S.M., and Wieschaus, E.F. (2000). Dynein-mediated cargo transport in
863 vivo. A switch controls travel distance. J Cell Biol *148*, 945-956.
864 Guglielmi, G., Barry, J.D., Huber, W., and De Renzis, S. (2015). An Optogenetic Method to Modulate Cell
865 Contractility during Tissue Morphogenesis. Dev Cell *35*, 646-660.
866 Hamelin, E., Theriault, C., Laroche, G., and Parent, J.L. (2005). The intracellular trafficking of the G
867 protein-coupled receptor TPbeta depends on a direct interaction with Rab11. J Biol Chem *280*, 36195-
868 36205.
869 Heald, R., Tournebize, R., Blank, T., Sandaltzopoulos, R., Becker, P., Hyman, A., and Karsenti, E. (1996).
870 Self-organization of microtubules into bipolar spindles around artificial chromosomes in Xenopus egg
871 extracts. Nature *382*, 420-425.
872 Hunyady, L., Baukal, A.J., Gaborik, Z., Olivares-Reyes, J.A., Bor, M., Szaszak, M., Lodge, R., Catt, K.J., and
873 Balla, T. (2002). Differential PI 3-kinase dependence of early and late phases of recycling of the
874 internalized AT1 angiotensin receptor. J Cell Biol *157*, 1211-1222.
875 Innamorati, G., Le Gouill, C., Balamotis, M., and Birnbaumer, M. (2001). The long and the short cycle.
876 Alternative intracellular routes for trafficking of G-protein-coupled receptors. J Biol Chem *276*, 13096-
877 13103.
878 Izquierdo, E., Quinkler, T., and De Renzis, S. (2018). Guided morphogenesis through optogenetic
879 activation of Rho signalling during early Drosophila embryogenesis. Nat Commun *9*, 2366.
880 Jha, A., van Zanten, T.S., Philippe, J.M., Mayor, S., and Lecuit, T. (2018). Quantitative Control of GPCR
881 Organization and Signaling by Endocytosis in Epithelial Morphogenesis. Curr Biol *28*, 1570-1584 e1576.
882 Jouette, J., Guichet, A., and Claret, S.B. (2019). Dynein-mediated transport and membrane trafficking
883 control PAR3 polarised distribution. Elife *8*.
884 Kerridge, S., Munjal, A., Philippe, J.M., Jha, A., de las Bayonas, A.G., Saurin, A.J., and Lecuit, T. (2016).
885 Modular activation of Rho1 by GPCR signalling imparts polarized myosin II activation during
886 morphogenesis. Nat Cell Biol *18*, 261-270.
887 Khanal, I., Elbediwy, A., Diaz de la Loza Mdel, C., Fletcher, G.C., and Thompson, B.J. (2016). Shot and
888 Patronin polarise microtubules to direct membrane traffic and biogenesis of microvilli in epithelia. J Cell
889 Sci *129*, 2651-2659.
890 Khodjakov, A., Copenagle, L., Gordon, M.B., Compton, D.A., and Kapoor, T.M. (2003). Minus-end capture
891 of preformed kinetochore fibers contributes to spindle morphogenesis. J Cell Biol *160*, 671-683.
892 Ko, C.S., Tserunyan, V., and Martin, A.C. (2019). Microtubules promote intercellular contractile force
893 transmission during tissue folding. J Cell Biol *218*, 2726-2742.
894 Laan, L., Pavin, N., Husson, J., Romet-Lemonne, G., van Duijn, M., Lopez, M.P., Vale, R.D., Julicher, F.,
895 Reck-Peterson, S.L., and Dogterom, M. (2012). Cortical dynein controls microtubule dynamics to
896 generate pulling forces that position microtubule asters. Cell *148*, 502-514.
897 Langevin, J., Morgan, M.J., Sibarita, J.B., Aresta, S., Murthy, M., Schwarz, T., Camonis, J., and Bellaiche, Y.
898 (2005). Drosophila exocyst components Sec5, Sec6, and Sec15 regulate DE-Cadherin trafficking from
899 recycling endosomes to the plasma membrane. Dev Cell *9*, 365-376.
900 Le Droguen, P.M., Claret, S., Guichet, A., and Brodu, V. (2015). Microtubule-dependent apical restriction
901 of recycling endosomes sustains adherens junctions during morphogenesis of the Drosophila tracheal
902 system. Development *142*, 363-374.
903 Lee, J.Y., and Harland, R.M. (2010). Endocytosis is required for efficient apical constriction during
904 Xenopus gastrulation. Curr Biol *20*, 253-258.
905 Letizia, A., Sotillos, S., Campuzano, S., and Llimargas, M. (2011). Regulated Crb accumulation controls
906 apical constriction and invagination in Drosophila tracheal cells. J Cell Sci *124*, 240-251.

907 Li, M., McGrail, M., Serr, M., and Hays, T.S. (1994). Drosophila cytoplasmic dynein, a microtubule motor
908 that is asymmetrically localized in the oocyte. J Cell Biol *126*, 1475-1494.
909 Lord, S.J., Velle, K.B., Mullins, R.D., and Fritz-Laylin, L.K. (2020). SuperPlots: Communicating
910 reproducibility and variability in cell biology. J Cell Biol *219*.
911 Manning, A.J., Peters, K.A., Peifer, M., and Rogers, S.L. (2013). Regulation of epithelial morphogenesis by
912 the G protein-coupled receptor mist and its ligand fog. Sci Signal *6*, ra98.
913 Manning, A.J., and Rogers, S.L. (2014). The Fog signaling pathway: insights into signaling in
914 morphogenesis. Dev Biol *394*, 6-14.
915 Martin, A.C., and Goldstein, B. (2014). Apical constriction: themes and variations on a cellular
916 mechanism driving morphogenesis. Development *141*, 1987-1998.
917 Martin, A.C., Kaschube, M., and Wieschaus, E.F. (2009). Pulsed contractions of an actin-myosin network
918 drive apical constriction. Nature *457*, 495-499.
919 Mason, F.M., Tworoger, M., and Martin, A.C. (2013). Apical domain polarization localizes actin-myosin
920 activity to drive ratchet-like apical constriction. Nat Cell Biol *15*, 926-936.
921 Meresse, S., Gorvel, J.P., and Chavrier, P. (1995). The rab7 GTPase resides on a vesicular compartment
922 connected to lysosomes. J Cell Sci *108 ( Pt 11)*, 3349-3358.
923 Miao, H., Vanderleest, T.E., Jewett, C.E., Loerke, D., and Blankenship, J.T. (2019). Cell ratcheting through
924 the Sbf RabGEF directs force balancing and stepped apical constriction. J Cell Biol.
925 Myat, M.M., and Andrew, D.J. (2000). Organ shape in the Drosophila salivary gland is controlled by
926 regulated, sequential internalization of the primordia. Development *127*, 679-691.
927 Myat, M.M., and Andrew, D.J. (2002). Epithelial tube morphology is determined by the polarized growth
928 and delivery of apical membrane. Cell *111*, 879-891.
929 Ossipova, O., Kim, K., Lake, B.B., Itoh, K., Ioannou, A., and Sokol, S.Y. (2014). Role of Rab11 in planar cell
930 polarity and apical constriction during vertebrate neural tube closure. Nat Commun *5*, 3734.
931 Rauzi, M., Lenne, P.F., and Lecuit, T. (2010). Planar polarized actomyosin contractile flows control
932 epithelial junction remodelling. Nature *468*, 1110-1114.
933 Riggs, B., Rothwell, W., Mische, S., Hickson, G.R., Matheson, J., Hays, T.S., Gould, G.W., and Sullivan, W.
934 (2003). Actin cytoskeleton remodeling during early Drosophila furrow formation requires recycling
935 endosomal components Nuclear-fallout and Rab11. J Cell Biol *163*, 143-154.
936 Roeth, J.F., Sawyer, J.K., Wilner, D.A., and Peifer, M. (2009). Rab11 helps maintain apical crumbs and
937 adherens junctions in the Drosophila embryonic ectoderm. PLoS One *4*, e7634.
938 Rogers, S.L., Wiedemann, U., Hacker, U., Turck, C., and Vale, R.D. (2004). Drosophila RhoGEF2 associates
939 with microtubule plus ends in an EB1-dependent manner. Curr Biol *14*, 1827-1833.
940 Roper, K. (2012). Anisotropy of Crumbs and aPKC drives myosin cable assembly during tube formation.
941 Dev Cell *23*, 939-953.
942 Royou, A., Field, C., Sisson, J.C., Sullivan, W., and Karess, R. (2004). Reassessing the role and dynamics of
943 nonmuscle myosin II during furrow formation in early Drosophila embryos. Mol Biol Cell *15*, 838-850.
944 Sanchez-Corrales, Y.E., Blanchard, G.B., and Roper, K. (2018). Radially patterned cell behaviours during
945 tube budding from an epithelium. Elife *7*.
946 Sawyer, J.M., Harrell, J.R., Shemer, G., Sullivan-Brown, J., Roh-Johnson, M., and Goldstein, B. (2010).
947 Apical constriction: a cell shape change that can drive morphogenesis. Dev Biol *341*, 5-19.
948 Sherwood, N.T., Sun, Q., Xue, M., Zhang, B., and Zinn, K. (2004). Drosophila spastin regulates synaptic
949 microtubule networks and is required for normal motor function. PLoS Biol *2*, e429.
950 Sidor, C., Stevens, T.J., Jin, L., Boulanger, J., and Roper, K. (2020). Rho-Kinase Planar Polarization at
951 Tissue Boundaries Depends on Phospho-regulation of Membrane Residence Time. Dev Cell *52*, 364-378
952 e367.
953 Takeda, M., Sami, M.M., and Wang, Y.C. (2018). A homeostatic apical microtubule network shortens
954 cells for epithelial folding via a basal polarity shift. Nat Cell Biol *20*, 36-45.

955 Tan, R., Foster, P.J., Needleman, D.J., and McKenney, R.J. (2018). Cooperative Accumulation of Dynein-
956 Dynactin at Microtubule Minus-Ends Drives Microtubule Network Reorganization. Dev Cell *44*, 233-247
957 e234.
958 Ullrich, O., Reinsch, S., Urbe, S., Zerial, M., and Parton, R.G. (1996). Rab11 regulates recycling through
959 the pericentriolar recycling endosome. J Cell Biol *135*, 913-924.
960 Urbansky, S., Gonzalez Avalos, P., Wosch, M., and Lemke, S. (2016). Folded gastrulation and T48 drive
961 the evolution of coordinated mesoderm internalization in flies. Elife *5*.
962 Volpicelli, L.A., Lah, J.J., Fang, G., Goldenring, J.R., and Levey, A.I. (2002). Rab11a and myosin Vb regulate
963 recycling of the M4 muscarinic acetylcholine receptor. J Neurosci *22*, 9776-9784.
964 Westermann, S., and Weber, K. (2003). Post-translational modifications regulate microtubule function.
965 Nat Rev Mol Cell Biol *4*, 938-947.
966 Wichmann, H., Hengst, L., and Gallwitz, D. (1992). Endocytosis in yeast: evidence for the involvement of
967 a small GTP-binding protein (Ypt7p). Cell *71*, 1131-1142.
968 Wodarz, A., Grawe, F., and Knust, E. (1993). CRUMBS is involved in the control of apical protein targeting
969 during Drosophila epithelial development. Mech Dev *44*, 175-187.
970 Yvon, A.M., Gross, D.J., and Wadsworth, P. (2001). Antagonistic forces generated by myosin II and
971 cytoplasmic dynein regulate microtubule turnover, movement, and organization in interphase cells. Proc
972 Natl Acad Sci U S A *98*, 8656-8661.
973 Zhang, J., Schulze, K.L., Hiesinger, P.R., Suyama, K., Wang, S., Fish, M., Acar, M., Hoskins, R.A., Bellen,
974 H.J., and Scott, M.P. (2007). Thirty-one flavors of Drosophila rab proteins. Genetics *176*, 1307-1322.
975 Zhang, X.M., Ellis, S., Sriratana, A., Mitchell, C.A., and Rowe, T. (2004). Sec15 is an effector for the Rab11
976 GTPase in mammalian cells. J Biol Chem *279*, 43027-43034.

977

**Figure S1. Rab11-EYFP, Rab5-EYFP and Sec15 are apically enriched in the invaginating SG.** (A-A'') *Rab11-EYFP* (an EYFP insertion at the N-terminus under the control of Rab11 regulatory sequences) SG labeled with antibodies against E-Cad (A), GFP (A') and Nuf (A''). (A'''-A'''''') Corresponding heat maps for apical areas of SG cells (A''') and intensities of GFP (A'''') and Nuf (A''''') signals. (B, B') Confocal images of a *Rab5-EYFP* (an EYFP insertion at the N-terminus under the control of Rab5 regulatory sequences) SG stained for E-Cad (B) and GFP (B'). (B'', B''') Corresponding heat maps for apical areas of SG cells (B'') and intensity of Rab5-EYFP signals (B'''). (C) Negative correlation between Rab5-EYFP intensity and apical areas of SG cells (n= 4 SGs; 396 cells). (D-D') *Rab7-EYFP* (an EYFP insertion at the N-terminus under the control of Rab7 regulatory sequences) SG immunostained for E-Cad (D) and GFP (D'). (D'', D''') Corresponding heat maps for apical areas of SG cells (D'') and intensity of Rab7-EYFP (D'''). (E-E''') Wild type SG immunostained for E-Cad (E) and Sec15 (E'). (E'', E''') Corresponding heat maps for apical areas of SG cells (E'') and intensity of Sec15 signals (E'''). (F) Negative correlation between the intensity of Sec15 and apical areas of SG cells (n= 5 SGs; 527 cells). Asterisks: invagination pit. White lines, SG boundary.

## Supplemental Figure 1

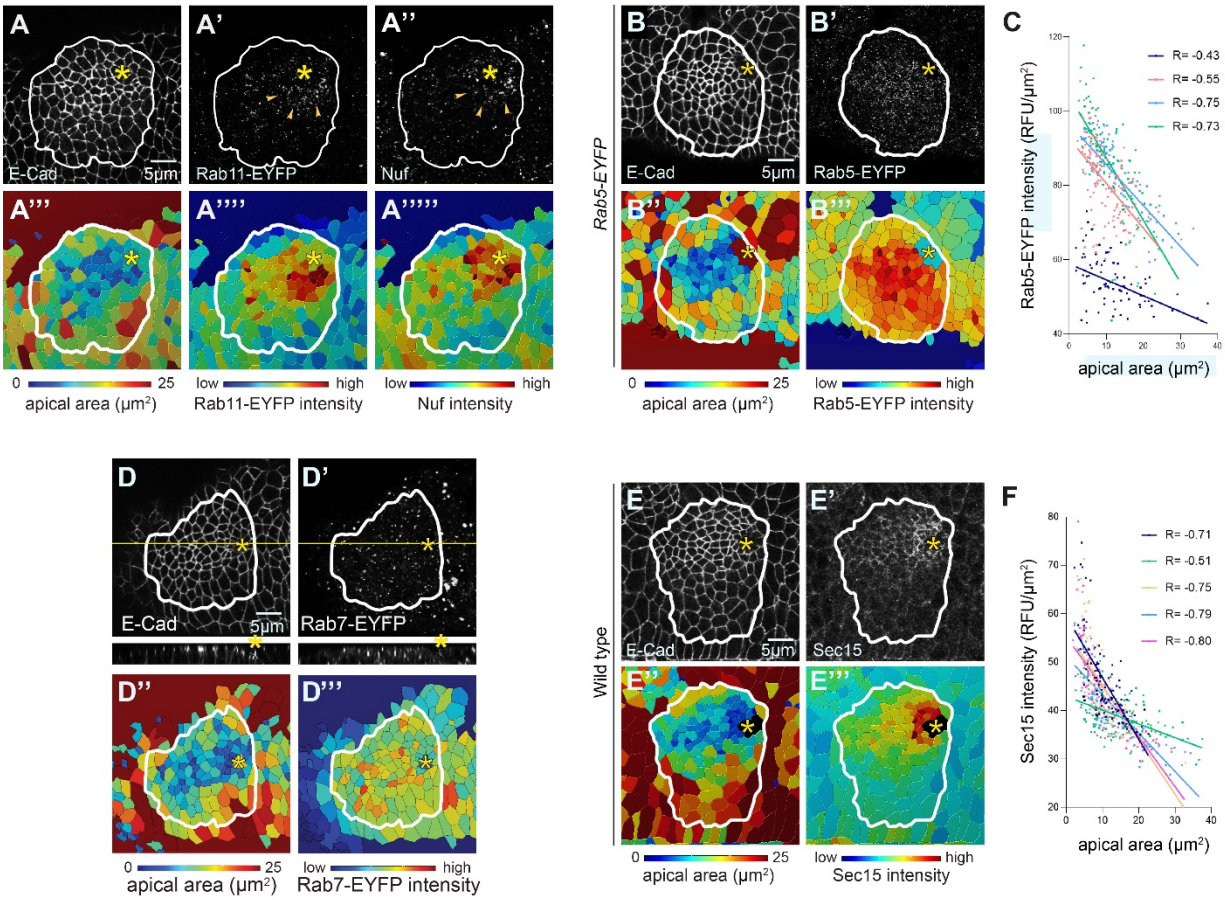

**Figure S2. Overexpression of spastin in the SG results in loss of acetylated-α-tubulin.** (A-B'') Confocal images of control (A-A'') and spastin-CFP-overexpressing (B-B'') SGs stained for phalloidin (red) and an antibody against acetylated α-tubulin (Ace-α-Tub; magenta). Spastin-CFP (green) signals show SG-specific overexpression of spastin by *fkh-Gal4*, which leads to a loss of MTs in the SG placode. Asterisks, invagination pit. (C-D) Confocal images of control (C) and spastin-overexpressing (D) SGs immunostained for E-Cad. (C'-D') Corresponding heat maps for apical areas in SGs in C and D. (E) Percentage and cumulative percentage of cells with different apical areas. Mann-Whitney U test (percentage of cells) and Kolmogorov-Smirnov test (cumulative percentage of cells). n= 5 SGs (control, 517 cells; spastin overexpression, 549 cells). *, $p<0.05$; **, $p<0.01$. Asterisks: invagination pit. White lines: SG boundary.

## Supplemental Figure 2

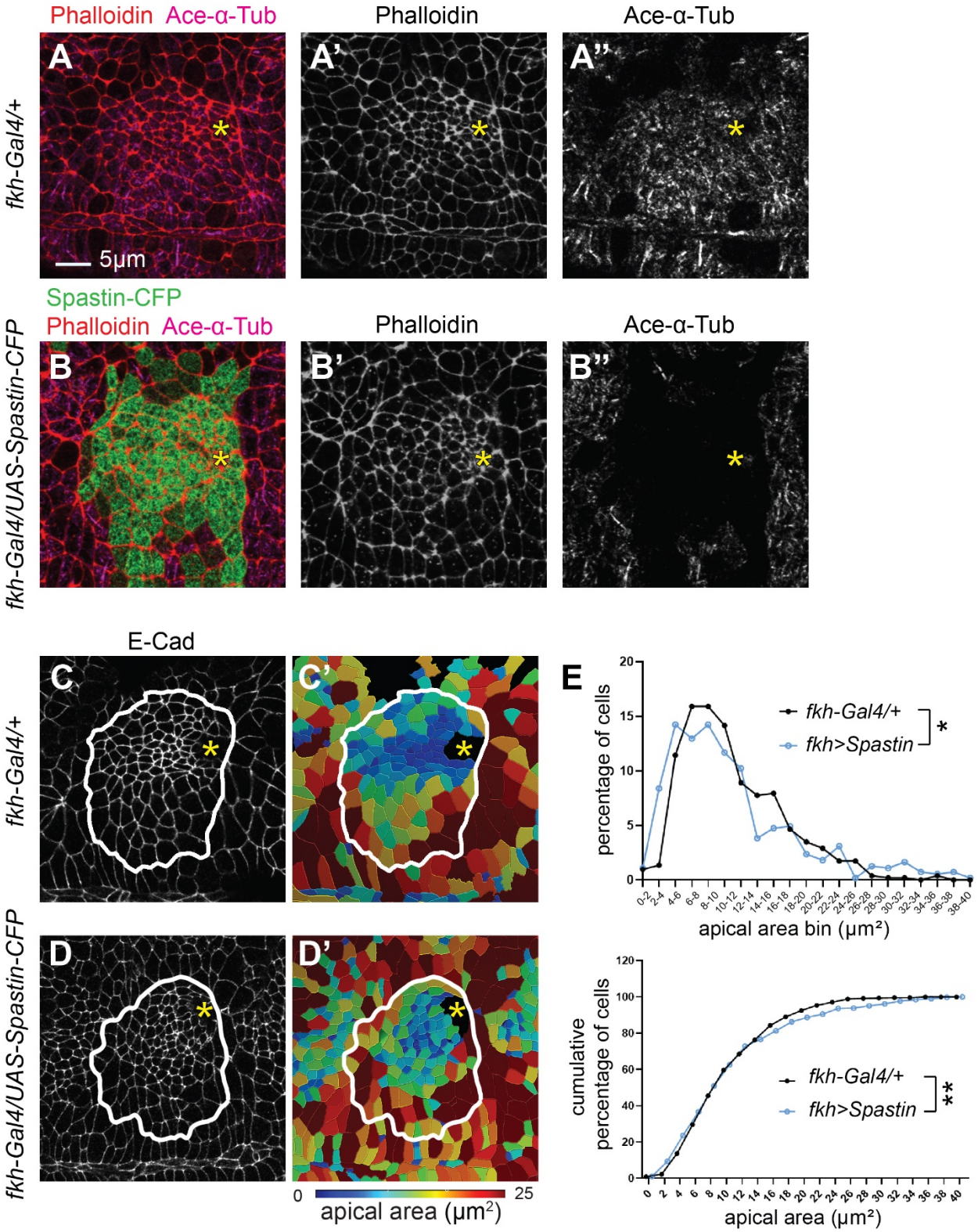

**Figure S3. Verification of RNAi knockdown in the SG.** (A-D') Control (A-B') and *Rab11* RNAi (C-D') SGs immunostained for Sage (SG nuclei) and Rab11. Stage 11 (A, A', C, C') and stage 13 (B, B', D, D') SGs are shown. (E, E') Stage 11 control (E) and *crb* RNAi (C-D') SGs immunostained for Crb. (E'') Quantification of the junctional intensity of Crb. (F, F') Stage 11 control (E) and *E-Cad* RNAi (C-D') SGs immunostained for E-Cad. (F'') Quantification of the junctional intensity of E-Cad. n= 5 SGs for both in E'' and F''; 10 cells in the dorsal/posterior region of each SG. **, $p < 0.01$ (Welch's t-test). Asterisks, invagination pit.

## Supplemental Figure 3

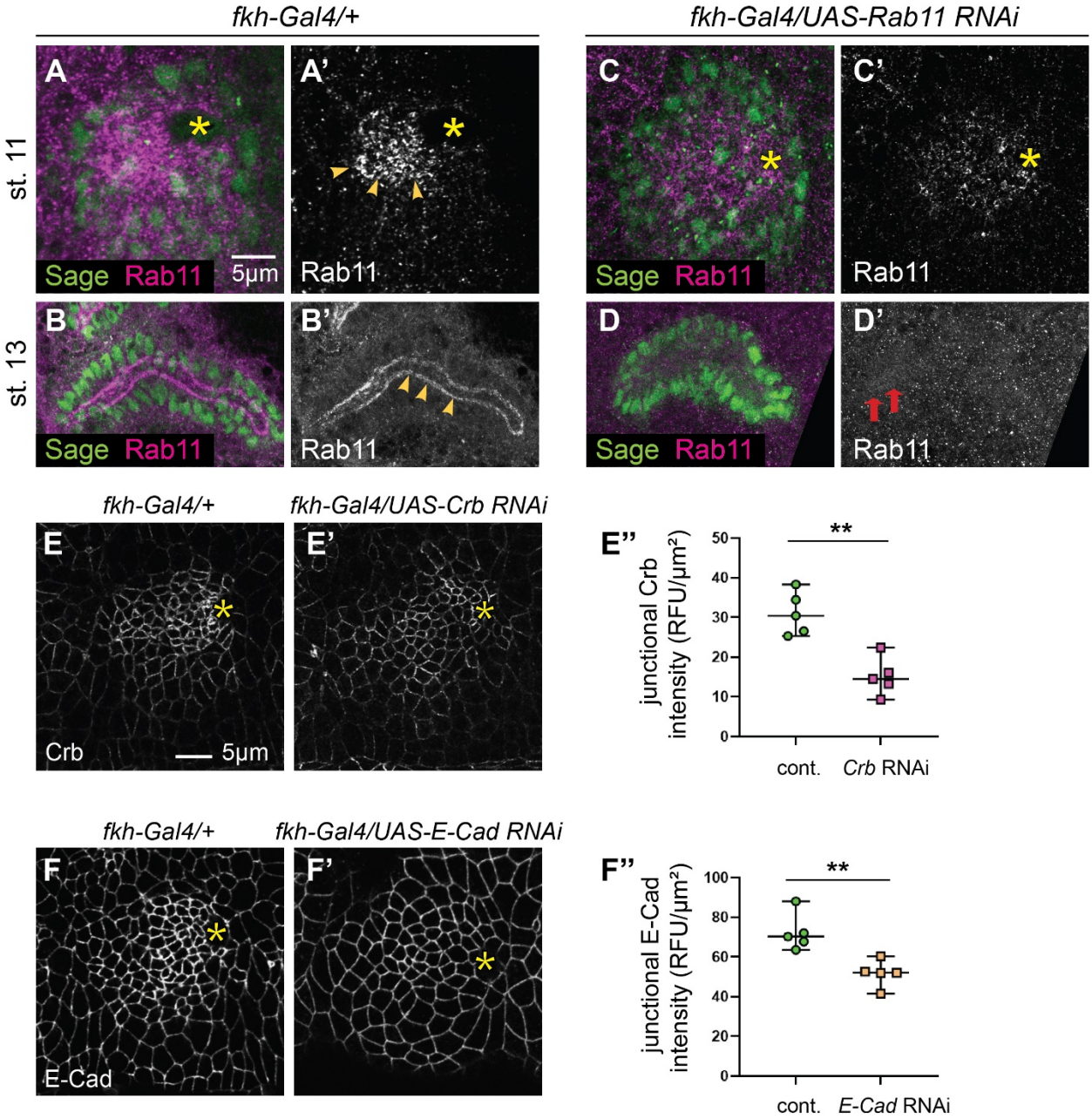

**Figure S4. MTs play a role in apical localization of Rab11 and apical transport of Crb and E-Cad throughout SG formation.** (A-B’’’) Confocal images of stage 16 control (A-A’’’) and spastin-overexpressing (B-B’’’) SGs immunostained for Rab11 and Nuf. In control, Rab11 and Nuf localize in the apical region of SG cells (red arrowheads in A’’ and A’’’). In spastin-overexpressing SGs, Rab11 and Nuf are mislocalized to aggregates in the cytoplasm of cells (yellow arrowheads in B’-B’’’). (C-E’’) Confocal images of stage 13 control (C-C’’), spastin-overexpressing (D-D’’) and *Rab11* RNAi (E-E’’) SGs immunostained for Sage (SG nuclei), E-Cad and Fog. (C’-E’) Compared to strong E-Cad signals primarily at adherens junctions in the control SG (C’), strong lateral E-Cad signals are shown in spastin-overexpressing and *Rab11* RNAi SG (blue arrows in E’). Insets, higher magnification of the yellow boxed regions in C’-E’. (C’’-E’’) Compared to strong apical Fog signals in the control SG (C’’), Fog signals are faint in spastin-overexpressing (D’’) and *Rab11* RNAi (E’’) SGs. (F-G’’’) Confocal images of stage 16 SGs stained for Crb and Rab11. (F-F’’’) Overexpression of Crb causes mislocalization of Crb (green) to all membrane domains and expands membranes. Rab11 is still enriched in the apical domain (red arrowheads). (G-G’’’) Co-overexpression of spastin and Crb results in mislocalization of Crb to large aggregates in the cytoplasm, which overlap with Rab11 (yellow arrowheads). (H-I’’’) Confocal images of stage 16 SGs immunostained for E-Cad and Rab11. (H-H’’’) In the control SG, the majority of E-Cad signals are detected at adherens junctions (red arrowheads). Small punctate E-Cad signals are occasionally shown in the basolateral region (blue arrows). (I-I’’’) Co-overexpression of E-Cad and spastin causes mislocalization of E-Cad to cytoplasmic aggregates, which overlap with Nuf (yellow arrowheads). White dashed line, cell and nuclear boundaries (A’, B’) and apical membrane (F’, H’, I’). Nu, nucleus.
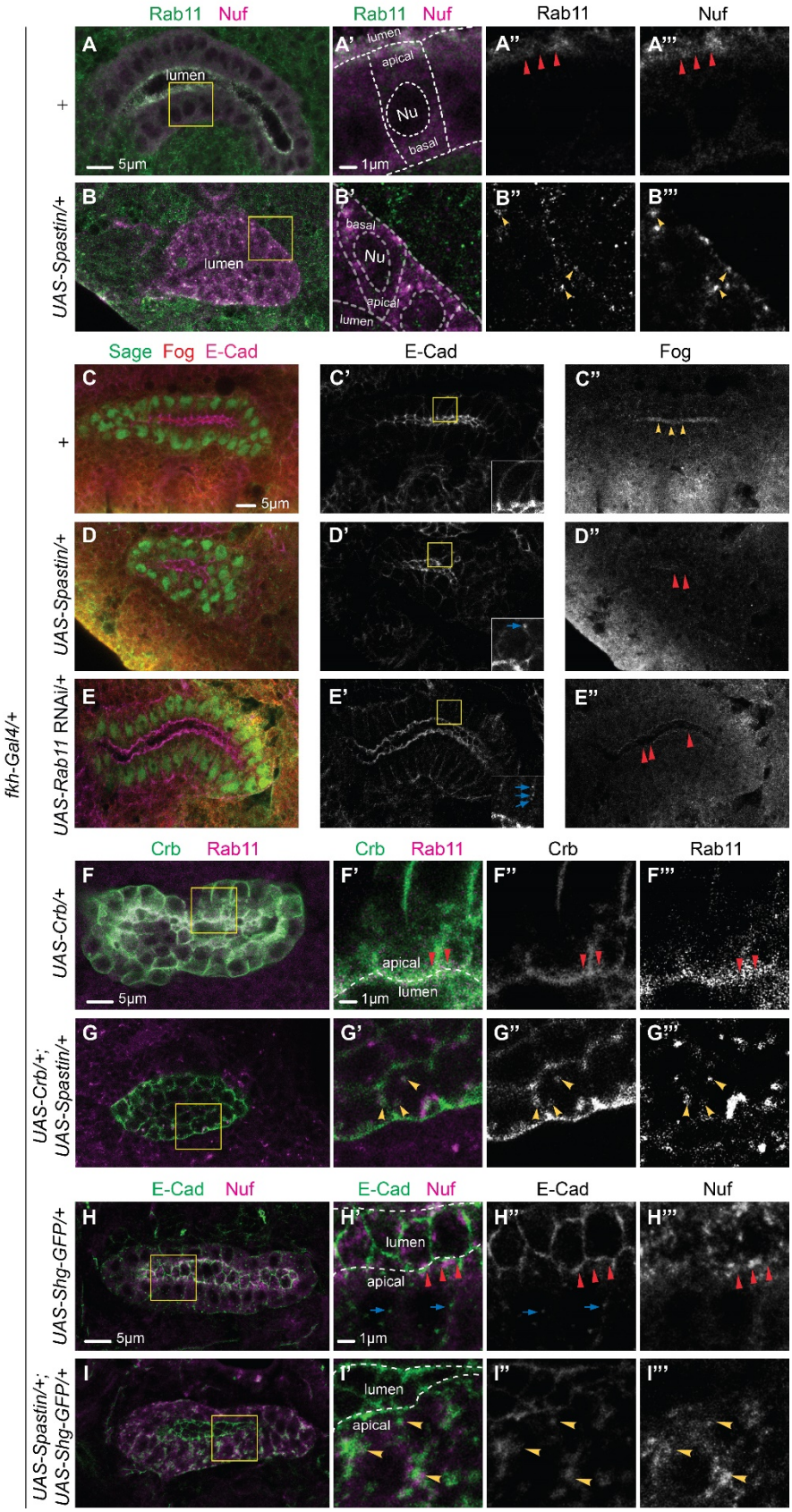
## Supplemental Figure 4